Kooiker, Sicco; van Brummelen, Janneke; Schaumburg, Julia; Zamojski, Marcin

Working Paper

Self-driving neural networks for term structure modeling

Tinbergen Institute Discussion Paper, No. TI 2026-007/III

Provided in Cooperation with:
Tinbergen Institute, Amsterdam and Rotterdam

Suggested Citation: Kooiker, Sicco; van Brummelen, Janneke; Schaumburg, Julia; Zamojski, Marcin (2026) : Self-driving neural networks for term structure modeling, Tinbergen Institute Discussion Paper, No. TI 2026-007/III, Tinbergen Institute, Amsterdam and Rotterdam

This Version is available at:
https://hdl.handle.net/10419/339244

TI 2026-007/III
Tinbergen Institute Discussion Paper

Self-driving neural networks for term structure modeling

Sicco Kooiker[1]
Janneke van Brummelen[2]
Julia Schaumburg[3]
Marcin Zamojski[4]

1 Vrije Universiteit Amsterdam

2 Vrije Universiteit Amsterdam, Tinbergen Institute

3 Vrije Universiteit Amsterdam, Tinbergen Institute

4 Vrije Universiteit Amsterdam

Self-driving neural networks for term structure modeling*

Sicco Kooiker[(a)] *Janneke van Brummelen*[(a,b)]

Julia Schaumburg[(a,b)] *Marcin Zamojski*[(a)]

[(a)] Vrije Universiteit Amsterdam [(b)] Tinbergen Institute

January 2026

Abstract

We propose a factor model with time-varying loadings for term structure modeling and forecasting. While maintaining the interpretation of the factors as level, slope, and curvature through explicit identification restrictions, we allow the loadings to take flexible shapes by specifying them as neural networks that evolve over time using a "self-driving" updating scheme based on past forecast errors, with gradient scaling to improve robustness. Using an empirically calibrated simulation study and an application to U.S. Treasury yields across 24 maturities, we show that flexible and dynamic factor loadings improve forecasting performance relative to standard benchmarks, including Nelson–Siegel models and the random walk. The gains are strongest at medium maturities and shorter forecast horizons, highlighting the importance of capturing curvature dynamics. In-sample results further illustrate how time-varying loadings provide insight into changes in yield curve shape beyond traditional parametric specifications.

Keywords: time-varying neural networks, observation-driven dynamics, yield curve.

*Email addresses: journal@zamojski.net (Marcin Zamojski), j.schaumburg@vu.nl (Julia Schaumburg), j.n.van.brummelen@vu.nl (Janneke van Brummelen), s.h.kooiker@vu.nl (Sicco Kooiker). Schaumburg and Kooiker thank the Dutch Science Foundation (NWO, grant VI.VIDI.191.169) for financial support. The estimation of the models was carried out using the the Dutch National supercomputer Snellius at SURF and the Ada cluster (formerly Bazis) at the Vrije Universitiet Amsterdam. We thank them for providing the computational resources.

1 Introduction

Accurate modeling and forecasting of the yield curve is crucial in finance and macroeconomics. Bond portfolio management, risk management, and pricing of derivatives all rely on accurate predictions of interest rates both in the time dimension and in the cross-section. The yield curve also sheds light on how monetary policy affects inflationary expectations of agents, depending on the state of the economy.

In practice, the most widely used bond yield forecasting models are linear. They include, on the one hand, dynamic factor models in the spirit of Nelson and Siegel (1987), see, for instance, Diebold et al. (2005), Diebold and Li (2006), Christensen et al. (2011), and Koopman et al. (2010). On the other hand, predictive regressions using principal components as proposed in Stock and Watson (2002) provide a simple yet powerful dimension reduction method to forecast bond yields. Even though linear models are often computationally inexpensive, while delivering interpretable outcomes and good forecasting performance, more complex nonlinear approaches have recently gained popularity in the asset pricing literature.[1] In particular, Bianchi et al. (2021) show in a comparative study that even shallow neural networks are able to predict bond excess returns significantly more accurately than their linear benchmarks.

In this paper, we introduce a new factor model with a time-varying loading matrix that is particularly useful for modeling and forecasting term structure data. We allow the factor loadings to take flexible, maturity-dependent shapes by specifying them as neural networks with time-varying weights. In contrast to Bianchi et al. (2021), we focus on forecasting the yield curve itself rather than excess returns. To accommodate the ordered cross-sectional structure of yields across maturities, we impose explicit identification restrictions that ensure the interpretability of the factors as level, slope, and curvature. The dynamics of both loading coefficients and latent factors are specified as functions of past observations. In particular, we follow Creal

[1] There is a growing literature focusing on modeling stock returns using neural networks, for example, Gu et al. (2020), Chen et al. (2024), Avramov et al. (2023), Gu et al. (2021)

et al. (2024) in using the influence function of a conditional moments-based objective function as the driving variable of our time-varying parameters. Our approach is computationally fast despite the inherently nonlinear nature of the underlying neural networks. The derivatives are calculated using automatic differentiation as proposed in Zamojski (2019), which only requires a criterion function as input and efficiently produces exact gradients, as opposed to numerical differentiation.

In an empirically calibrated simulation study as well as in an extensive application to U.S. Treasury yields, we show that allowing for flexible and dynamic factor loadings improves out-of-sample forecasting performance relative to static factor models and widely used benchmarks. The gains are particularly strong when the loading dynamics are combined with gradient scaling, which improves robustness to large past forecast errors. In the empirical application, the most flexible specification—a scaled self-driving neural network model with heterogeneous coefficients—consistently appears among the best-performing models across maturities and forecast horizons, while benchmark models do not. Our approach outperforms the benchmarks particularly strongly at medium maturities, which are associated with the curvature of the yield curve.

Our framework can be viewed as a flexible generalization of the (dynamic) Nelson-Siegel class of models (Nelson and Siegel, 1987; Diebold and Li, 2006; Diebold et al., 2005). While we preserve the economic interpretation of the factors, replacing the static exponential basis functions in the loading matrix with time-varying neural networks allows the model to accommodate both gradual and abrupt changes in the dynamics of the yield curve that may arise due to economic shocks or monetary policy adjustments. Indeed, our in-sample analysis suggests that allowing the loading functions to evolve over time, i.e. disentangling changes in the yield curve's shape from movements in the factors themselves, offers a richer interpretation than is possible under the Nelson–Siegel parametrization.

Beyond yield curve modeling, our approach also relates to the broader literature on fac-

tor models with time-varying loadings. In the context of predicting macroeconomic variables, factor models with constant loadings are very common, including static factors based on principal components (e.g., Stock and Watson, 2002; Bai and Ng, 2013, and many others) and dynamic versions using state space methods that are estimated with either Bayesian (Kose et al., 2003; Bernanke et al., 2003; Bai and Wang, 2015) or frequentist procedures (Doz et al., 2012; Jungbacker and Koopman, 2015; Barigozzi and Luciani, 2024). Several papers have proposed extensions to the classical factor model approach to allow for dynamics in the coefficients. The need for these modifications stems from potential instability of models over time due to, e.g., changes in market environments and monetary policy. For instance, Del Negro and Otrok (2008) study changes in international business cycles. They specify loading coefficients and variances as random walks and propose a Gibbs sampling technique for filtering and estimation. Mikkelsen et al. (2019), on the other hand, cast the factor model in a state space form, first extract principal components based on constant loadings, and then estimate separate vector autoregressions for each row of the loading matrix. Su and Wang (2017) model factor loadings as a smooth function of time, giving rise to local principal components, and Cheung (2024) formally studies identification conditions for factor models based on such local principal components and time-varying loadings. In contrast to these settings, our application to term structure data exploits the ordered maturity structure and economically motivated level, slope, and curvature interpretation to impose point-in-time identification restrictions, which resolve the rotation and sign indeterminacy that commonly affects factor models with latent time-varying loadings.

The remainder of the paper is organized as follows. Section 2 presents the neural network factor model, the dynamic updating equations for both the factors and the loading matrix, and the transformations used to achieve unique identification and economic interpretability. Section 3 presents an empirically calibrated simulation study that illustrates the behavior of the proposed model under different types of time-variation and compares it to alternatives based on the Nelson-Siegel specification. Section 4 presents an empirical application to U.S. yield data

across 24 maturities, including both a comprehensive out-of-sample forecasting evaluation and in-sample analysis. Section 5 concludes.

2 Methodology

2.1 Neural Factor Model

Let $\boldsymbol{y}_t = (y_{1t}, \ldots, y_{Nt})'$ denote a vector of zero-coupon yields observed at the maturities $\boldsymbol{\tau} = (\tau_1, \ldots, \tau_N)'$ with $0 < \tau_1 < \cdots < \tau_N$. We assume that yields are represented by a K-factor model

$$\boldsymbol{y}_t = \Gamma(\boldsymbol{\tau}; \boldsymbol{\gamma}_t)\, \boldsymbol{\beta}_t + \boldsymbol{\varepsilon}_t, \tag{1}$$

where $K \leq N$, $\boldsymbol{\beta}_t \in \mathbb{R}^K$ collects the factors, and $\Gamma(\boldsymbol{\tau}; \boldsymbol{\gamma}_t) \in \mathbb{R}^{N \times K}$ is a loading matrix parametrised by $\boldsymbol{\gamma}_t$. The N-dimensional disturbance vector $\boldsymbol{\varepsilon}_t$ is serially independent with $\mathbb{E}[\boldsymbol{\varepsilon}_t] = \mathbf{0}$ and $\mathrm{Var}(\boldsymbol{\varepsilon}_t) = \sigma_t^2 \mathbf{I}_N$.

Each column of the loading matrix is generated by a different feed-forward neural network:

$$\Gamma_{ij}(\tau_i; \boldsymbol{\gamma}_t) = \mathrm{NN}(\tau_i; \boldsymbol{\gamma}_{jt}), \qquad i = 1, \ldots, N,\ j = 1, \ldots, K. \tag{2}$$

The specification of the single-layered neural network with L neurons is

$$\mathrm{NN}(\tau; \boldsymbol{\gamma}) = \sum_{l=1}^{L} w_{2l}\, \phi\big(w_{1l}\, \tau + b_l\big), \tag{3}$$

where $\phi : \mathbb{R} \to \mathbb{R}$ is an activation function (e.g., sigmoid, tanh, or ReLU) and the vector $\boldsymbol{\gamma} = (w_{11}, \ldots, w_{1L}, b_1, \ldots, b_L, w_{21}, \ldots, w_{2L},)' \in \mathbb{R}^{3L}$ collects the weights and biases. Stacking the parameters of the K networks gives the stacked vector $\boldsymbol{\gamma}_t = (\boldsymbol{\gamma}_{1t}', \ldots, \boldsymbol{\gamma}_{Kt}')'$. The neural networks are of the one-input, one-output type, i.e., $\mathrm{NN}(\cdot; \boldsymbol{\gamma}) : \mathbb{R}_+ \to \mathbb{R}$. The scalar maturity is the input and the corresponding factor loading is the output. Although deeper networks may be more parsimonious in specific applications, in our application to yield data a shallow

single-layer neural network is sufficiently parsimonious while flexible enough in representing the relation between the maturity and the loading.

REMARK 2.1: *While we specify the loading matrix using neural networks, alternative methods exist. For instance, the Nelson-Siegel model defines a static loading matrix that depends on a single shape parameter (see, e.g., Diebold and Li, 2006):*

$$\Gamma_{ij}^{NS}(\tau_i;\lambda) = \begin{cases} 1, & j=1, \\ \frac{1-e^{-\lambda\tau_i}}{\lambda\tau_i}, & j=2, \\ \frac{1-e^{-\lambda\tau_i}}{\lambda\tau_i} - e^{-\lambda\tau_i}, & j=3, \end{cases} \tag{4}$$

where $\lambda > 0$ is a parameter that governs the decay rate. There are a number of approaches for estimating λ and $\boldsymbol{\beta}_t$ in this model. The simplest is proposed by Diebold and Li (2006): given λ, the factors $\boldsymbol{\beta}_t$ are estimated using cross-sectional OLS at each time t, and then a VAR(p) model is fitted to forecast these factors. The yield forecasts are obtained by plugging the forecasted factors back into the model.

2.2 Unique Identification and Interpretability

In their current form, the factor loadings $\Gamma_t := \Gamma(\boldsymbol{\tau};\boldsymbol{\gamma}_t)$ and the factors $\boldsymbol{\beta}_t$ are not uniquely identified, because for any invertible matrix $Q \in \mathbb{R}^{K\times K}$ we have

$$\Gamma_t\boldsymbol{\beta}_t \;=\; \big(\Gamma_t Q\big)\big(Q^{-1}\boldsymbol{\beta}_t\big),$$

such that $\Gamma_t^\dagger = \Gamma_t Q$ and $\boldsymbol{\beta}_t^\dagger = Q^{-1}\boldsymbol{\beta}_t$ yield an observationally equivalent model. Furthermore, the filtered factors $\boldsymbol{\beta}_t$ are not directly interpretable. Identification and interpretability are common issues in factor model estimation. Stock and Watson (2016) thoroughly discuss this for a variety of factor models. We combine some of techniques they describe to achieve identification

and interpretability.

By appropriately transforming the output of the neural networks, we can simultaneously satisfy the identification requirements and obtain interpretable factors. We specify the transformation so that the factors correspond to the three ($K = 3$) Nelson-Siegel factors; namely, the *level*, *slope* and *curvature*. The requirements for this are:

$$\hat{y}_t(\tau_i) := y_{it}$$

$$\hat{y}_t(\tau_N) = \beta_{1t}, \qquad \textit{level}$$

$$\hat{y}_t(\tau_N) - \hat{y}_t(\tau_1) = -\beta_{2t}, \qquad \textit{slope}$$

$$[\hat{y}_t(\tau^*) - \hat{y}_t(\tau_1)] - [\hat{y}_t(\tau_N) - \hat{y}_t(\tau^*)] \approx \beta_{3t}, \qquad \textit{curvature}$$

for some intermediate value τ^*.

We begin by fixing the first column of Γ_t to be a vector of ones, which ensures that this column represents a uniform loading across all maturities. In addition, we impose the restrictions $\Gamma_{t,N2} = 0$ and $\Gamma_{t,N3} = 0$, so that the predicted yield at the longest maturity is determined solely by β_{1t}, which can therefore be interpreted as the level factor. Likewise, to capture the slope of the yield curve, we set $\Gamma_{t,12} = 1$ and $\Gamma_{t,13} = 0$, thereby tying $-\beta_{2t}$ to the difference between the shortest and longest maturities. To identify the curvature factor, we fix the Euclidean norm of the third column and require all elements of Γ_t to be nonnegative, which allows β_{3t} to be associated with the curvature in the yield curve. Finally, we need one more restriction to identify the loading matrix. We add this last restriction by setting the second-to-last entry of the second column to zero, i.e. $\Gamma_{t,(N-1)2} = 0$. This constraint has negligible impact on the interpretation of the factors but provides full identifiability of the model. Table 1 summarizes all imposed restrictions.

TABLE 1: Conditions for Unique Identification of Factor Loadings

Label	**Condition**
L-C1	$\Gamma_{t,i1} = 1$ for all $i = 1, \ldots, N$
S-C1	$\Gamma_{t,12} = 1$
S-C2	$\Gamma_{t,(N-1)2} = 0$
S-C3	$\Gamma_{t,N2} = 0$
C-C1	$\Gamma_{t,13} = 0$
C-C2	$\Gamma_{t,N3} = 0$
C-C3	$\sqrt{\sum_{i=1}^{N} \Gamma_{t,i3}^2} = 1$
C-C4	$\Gamma_{t,i3} > 0$ for all $i = 1, \ldots, N$

Proposition 2.1 below establishes that these conditions ensure identification of the factors and loadings.

PROPOSITION 2.1: *Under the restrictions in Table 1, Γ_t is uniquely identified. In particular, if Γ_t satisfies the restrictions, then any rotation $\Gamma_t^\dagger = \Gamma_t Q$ satisfies them only if $Q = I_3$.*

Proof. Suppose Γ_t satisfies the conditions in Table 1 and Q is such that $\Gamma_t^\dagger = \Gamma_t Q$ also satisfies these conditions. We proceed by going through $\Gamma_t^\dagger$ row by row, and examining the implications of the restrictions on Q. We let q_{ij} denote the (i, j)-th element of Q.

Step 1 (row N). By L-C1, S-C2, and C-C2, row N of Γ_t and $\Gamma_t^\dagger$ take the form $e_1 := (1, 0, 0)$. Thus, Q must be such that $e_1 = e_1 Q$, which yields the following equations:

$$1 = 1 \cdot q_{11} + 0 \cdot q_{21} + 0 \cdot q_{31}, \quad 0 = 1 \cdot q_{12} + 0 \cdot q_{22} + 0 \cdot q_{32}, \quad 0 = 1 \cdot q_{13} + 0 \cdot q_{23} + 0 \cdot q_{33}.$$

This directly implies that $q_{11} = 1$, $q_{12} = 0$, and $q_{13} = 0$, fixing the first row of Q.

Step 2 (row 1). By L-C1, S-C1, and C-C1, the first row of Γ_t and $\Gamma_t^\dagger$ takes the form

$g_1 := (1, 1, 0)$. Therefore, Q must be such that $g_1 = g_1 Q$, which yields the following equations:

$$1 = 1 \cdot q_{11} + 1 \cdot q_{21} + 0 \cdot q_{31}, \quad 1 = 1 \cdot q_{12} + 1 \cdot q_{22} + 0 \cdot q_{32}, \quad 0 = 1 \cdot q_{13} + 1 \cdot q_{23} + 0 \cdot q_{33}.$$

Using that $q_{11} = 1$, $q_{12} = 0$, and $q_{13} = 0$ by step 1, these equations imply that $q_{21} = 0$, $q_{22} = 1$, and $q_{23} = 0$. Thus, the second row of Q is also uniquely determined.

Step 3 (rows 2 to $N - 1$). Using conditions L-C1, S-C2, and C-C3, considering rows $i = 2, \ldots, N - 1$ of $\Gamma_t^\dagger = \Gamma_t Q$, gives the following equations

$$1 = 1 \cdot q_{11} + \Gamma_{t,i2} \cdot q_{21} + \Gamma_{t,i3} \cdot q_{31}, \quad \Gamma_{t,i2}^\dagger = 1 \cdot q_{12} + \Gamma_{t,i2} \cdot q_{22} + \Gamma_{t,i3} \cdot q_{32},$$

$$\Gamma_{t,i3}^\dagger = 1 \cdot q_{13} + \Gamma_{t,i2} \cdot q_{23} + \Gamma_{t,i3} \cdot q_{33}.$$

We saw in steps 1 and 2 that $q_{11} = 1$, $q_{12} = 0$, $q_{13} = 0$, $q_{21} = 0$, $q_{22} = 1$ and $q_{23} = 0$. Hence, because by C-C4 $\Gamma_{t,i3} > 0$, the first equation immediately implies $q_{31} = 0$. The second equation simplifies to $\Gamma_{t,i2}^\dagger = \Gamma_{t,i2} + \Gamma_{t,i3} \cdot q_{32}$. In particular, for $i = N - 1$ we know from condition S-C2 that $\Gamma_{t,(N-1)2} = 0$ and $\Gamma_{t,(N-1)2}^\dagger = 0$, which gives $0 = \Gamma_{t,(N-1)3} \cdot q_{32}$. Since $\Gamma_{t,(N-1)3} > 0$ by C-C4, we conclude $q_{32} = 0$. For the third equation, we have $\Gamma_{t,i3}^\dagger = \Gamma_{t,i3} \cdot q_{33}$. By the normalization condition C-C3 we therefore must have $|q_{33}| \sqrt{\sum_{i=1}^N \Gamma_{t,i3}^2} = 1$, from which it follows that $|q_{33}| = 1$, which by the positivity condition C-C4 implies that $q_{33} = 1$.

It follows that the restrictions are satisfied only for $Q = I_3$, which finishes the proof. □

2.3 Neural Network Transformations

Proposition 2.1 establishes identification under the conditions in Table 1. Enforcement of these restrictions—such that the neural networks specifying the factor loading matrix satisfy these conditions—can be accomplished in a number of ways. We propose an approach that satisfies all conditions and that we find to be computationally efficient. We refer to this set of transfor-

mations as the Neural Nelson–Siegel (NNS) transformations. We define the transformations of the neural networks as follows.

For the first neural network, we trivially set

$$\mathrm{NN}^*(\tau_i;\boldsymbol{\gamma}_1) = 1, \qquad \forall i = 1\dots N, \tag{5}$$

which ensures that L-C1 holds.

For the second neural network, we apply a linear rescaling and impose a fixed point to satisfy S-C1, S-C2, and S-C3:

$$\mathrm{NN}^*(\tau_i;\boldsymbol{\gamma}_2) \;=\; \frac{\mathrm{NN}(\tau_i;\boldsymbol{\gamma}_2) \;-\; \mathrm{NN}(\tau_N;\boldsymbol{\gamma}_2)}{\mathrm{NN}(\tau_1;\boldsymbol{\gamma}_2) \;-\; \mathrm{NN}(\tau_N;\boldsymbol{\gamma}_2)} \qquad \forall i = 1\dots N. \tag{6}$$

For the third neural network, we subtract the straight line connecting the outputs at the shortest and longest maturities from every output, anchoring those two maturities at zero to satisfy C-C1 and C-C2. We then square the results to ensure positivity and normalize the resulting vector by its Euclidean norm, which satisfies C-C3 and C-C4. These transformations restrict

$$\begin{aligned} \mathrm{NN}^\dagger(\tau_i;\boldsymbol{\gamma}_3) &= \Big(\mathrm{NN}(\tau_i;\boldsymbol{\gamma}_3) - \Big[\mathrm{NN}(\tau_1;\boldsymbol{\gamma}_3) + \tfrac{\mathrm{NN}(\tau_N;\boldsymbol{\gamma}_3)-\mathrm{NN}(\tau_1;\boldsymbol{\gamma}_3)}{\tau_N-\tau_1}(\tau_i-\tau_1)\Big]\Big)^2, \\ \mathrm{NN}^*(\tau_i;\boldsymbol{\gamma}_3) &= \mathrm{NN}^\dagger(\tau_i;\boldsymbol{\gamma}_3)\Big/\sqrt{\textstyle\sum_{i=1}^N \big(\mathrm{NN}^\dagger(\tau_i;\boldsymbol{\gamma}_3)\big)^2}, \qquad \forall i = 1\dots N. \end{aligned} \tag{7}$$

We emphasize that the proposed transformations of $\mathrm{NN}(\tau_i;\boldsymbol{\gamma}_2)$ and $\mathrm{NN}(\tau_i;\boldsymbol{\gamma}_3)$ ensure the identification of the loadings Γ_t and the factors $\boldsymbol{\beta}_t$, but do not imply the identification of the parameters $\boldsymbol{\gamma}_2$ and $\boldsymbol{\gamma}_3$. In particular, multiple parameter vectors $\boldsymbol{\gamma}_2$ and $\boldsymbol{\gamma}_3$ can yield identical transformed neural network functions. Although the neural network parameters are not uniquely identified, this does not compromise the identification of the factor structure, which is the object of interest in our analysis.

2.4 Estimation and filtering

To estimate the model in Equation (1), we filter the parameters $\boldsymbol{\gamma}$ that determine the loading matrix Γ_t using an observation-driven time-varying Generalized Method of Moments (tv-GMM) filter proposed by Creal et al. (2024) which extends the score-driven framework of Creal et al. (2013) to the method-of-moments setting. We specify the one-step-ahead predictions of $\boldsymbol{y}_t$ in the following way:

$$\widehat{\boldsymbol{y}}_t = \Gamma(\boldsymbol{\tau}; \widehat{\boldsymbol{\gamma}}_t)\, \widehat{\boldsymbol{\beta}}_t \;=\; \widehat{\Gamma}_t\, \widehat{\boldsymbol{\beta}}_t, \tag{8}$$

These predictions are built from the predicted factors and loadings, where $\widehat{\Gamma}_t$ and $\widehat{\boldsymbol{\beta}}_t$ denote the one-step-ahead predictions of $\Gamma(\boldsymbol{\tau}; \boldsymbol{\gamma}_t)$ and $\boldsymbol{\beta}_t$. For each time t we predict both. Because of the model's nonlinearity, we adopt a three-step procedure at each time point. First, we obtain the filtered state of the factors by a cross-sectional least-squares estimate:

$$\widetilde{\boldsymbol{\beta}}_{t|t} = \left(\widehat{\Gamma}_t' \widehat{\Gamma}_t\right)^{-1} \widehat{\Gamma}_t' \boldsymbol{y}_t. \tag{9}$$

This step requires the loading matrix estimate to be full rank. Second, we update the factor loadings using the tv-GMM filter, which uses the scaled gradient of the squared error loss function evaluated at time t, conditional on $\boldsymbol{\beta}_t = \widetilde{\boldsymbol{\beta}}_{t|t}$,

$$\widehat{\boldsymbol{\gamma}}_{t|t} = A \boldsymbol{s}_t + \widehat{\boldsymbol{\gamma}}_t, \tag{10}$$

$$\boldsymbol{s}_t = S_t^{-1} \nabla_t \tag{11}$$

$$\nabla_t = \frac{\partial}{\partial \boldsymbol{\gamma}_t} \left(\boldsymbol{y}_t - \Gamma_t \boldsymbol{\beta}_t\right)' \left(\boldsymbol{y}_t - \Gamma_t \boldsymbol{\beta}_t\right) \Big|_{\boldsymbol{\gamma}_t = \widehat{\boldsymbol{\gamma}}_t,\, \boldsymbol{\beta}_t = \widetilde{\boldsymbol{\beta}}_{t|t}}, \tag{12}$$

where $A \in \mathbb{R}^{3LK \times 3LK}$ is the learning-rate matrix, as larger entries lead to faster updating, and $\boldsymbol{s}_t$ represents the scaled update direction, where S_t scales the gradient ∇_t. The matrix A is a parameter that has to be estimated, our choice for the scaling matrix S_t is discussed in Section

2.5 and the gradient ∇_t does not have to be analytically derived, as it can be obtained using automatic differentiation, see Zamojski (2019). Third, to ensure that the factors minimize the cross-sectional squared error given the updated loadings, we recompute a least-squares estimate,

$$\widehat{\boldsymbol{\beta}}_{t|t} = \left(\widehat{\Gamma}'_{t|t}\widehat{\Gamma}_{t|t}\right)^{-1}\widehat{\Gamma}'_{t|t}\boldsymbol{y}_t. \tag{13}$$

We complete the recursion with the state predictions

$$\widehat{\boldsymbol{\beta}}_{t+1} = \boldsymbol{\omega}_1 + B_\beta\widehat{\boldsymbol{\beta}}_{t|t}, \qquad \widehat{\boldsymbol{\gamma}}_{t+1} = \boldsymbol{\omega}_2 + B_\gamma\widehat{\boldsymbol{\gamma}}_{t|t}, \tag{14}$$

where $\boldsymbol{\omega}_1 \in \mathbb{R}^K$, $B_\beta \in \mathbb{R}^{K\times K}$, $\boldsymbol{\omega}_2 \in \mathbb{R}^{3LK}$, and $B_\gamma \in \mathbb{R}^{3LK\times 3LK}$ are parameters to be estimated. The vectors $\boldsymbol{\omega}_1$ and $\boldsymbol{\omega}_2$ capture the unconditional means, while B_β and B_γ govern the speed of mean reversion.

Given the filtering procedure described above, the static parameters for a given sample of observations $\{\boldsymbol{y}_t\}_{t=1}^T$ are estimated by minimizing the sum of squared residuals:

$$\widehat{\boldsymbol{\theta}} = \arg\min_{\boldsymbol{\theta}} \sum_{t=1}^{T} (\boldsymbol{y}_t - \widehat{\Gamma}_t\widehat{\boldsymbol{\beta}}_t)'(\boldsymbol{y}_t - \widehat{\Gamma}_t\widehat{\boldsymbol{\beta}}_t), \tag{15}$$

where $\boldsymbol{\theta}$ collects all the static parameters, $\boldsymbol{\theta} = (\mathrm{vec}(A)', \boldsymbol{\omega}_1', \mathrm{vec}(B_\beta)', \boldsymbol{\omega}_2', \mathrm{vec}(B_\gamma)')'$. We refer to the model defined by Equations (8)–(15) as Self-Driving Neural Factor Model (SDNFM) to reflect not only its observation-driven nature, but also the implementation simplicity obtained by automatic differentiation as in Zamojski (2019).

The model naturally supports one-step-ahead out-of-sample forecasting. For a longer forecast horizon H, we skip Equations (9)–(13) by treating the last predictions as filtered estimates,

$$\widehat{\boldsymbol{\beta}}_{T+h|T+h} = \widehat{\boldsymbol{\beta}}_{T+h}, \qquad \widehat{\boldsymbol{\gamma}}_{T+h|T+h} = \widehat{\boldsymbol{\gamma}}_{T+h}, \qquad h = 1, \ldots, H-1.$$

In combination with Equations (8) and (14), we recursively get the predictions for $\boldsymbol{y}_{t+H}$.

2.5 Scaling

In the framework of Creal et al. (2024), the scaling matrix naturally arises as

$$\mathbb{E}_{t-1}\left[\frac{\partial \nabla_t}{\partial \gamma_t}\right],$$

where the expectation is taken with respect to the conditional distribution of $\mathbf{y}_t$ given $(\mathbf{y}_{t-1}, \ldots, \mathbf{y}_1)$. When this distribution is unknown, Creal et al. (2024) propose approximating it using an exponentially weighted moving average (EWMA) of recent derivatives of the gradient ∇_t.

In our setting, however, implementing this approach requires evaluating $(3LK)^2$ additional derivatives at each iteration of the filter. This quadratic growth in computational burden is a well-known challenge in neural network optimization and motivates the use of approximation schemes that require only first-order derivatives. RMSprop (Tieleman and Hinton, 2012), and its popular extension ADAM (Kingma and Ba, 2017), address this by replacing the expectation of second-order terms with an EWMA of squared gradients. Following this idea, we define the scaling matrix S_t using the following recursion for $i = 1, \ldots, 3LK$

$$P_{it} = \rho P_{i,t-1} + (1-\rho)\,\nabla_{it}^2, \tag{16}$$

$$S_{it} = \frac{1}{1-\rho^t}\sqrt{P_{it}} + \epsilon, \tag{17}$$

and $S_t = \text{diag}(S_{1t}, \ldots, S_{3LK,t})$, where $\rho \in (0,1)$ controls the update speed and ϵ is a small positive constant introduced to avoid division by zero. Instead of directly scaling by P_t, we use the ADAM-style bias correction shown in (17) (Kingma and Ba, 2017). This correction is necessary because P_0 is initialized at zero, which biases early values of P_t downward and can lead to unrealistically small scaling factors. Although ρ could in principle be optimized, doing so would impose substantial computational cost. We therefore set $\rho = 0.98$ to balance between

responsiveness to time-variation and robustness to noisy updates. As a benchmark, we also consider scaling with the identity matrix.

2.6 Model configurations

We now discuss which specific model configurations we use in the remainder of the paper. The model introduced in Section 2.4 is governed by the matrices A, $\boldsymbol{\omega}_1$, B_β, $\boldsymbol{\omega}_2$, B_γ and the scaling S_t. We set the number of latent factors to $K = 3$ and fix the size of each neural network at $L = 3$. Each of the models has uniquely identified factors and loadings by the NNS transformations. Without additional restrictions, this specification involves 1,497 free parameters. To contain estimation variance and reduce computing time we impose diagonality restrictions on A and B_γ. Table 2 summarizes four nested variants: NNS, 1SD-NNS, 2SD-NNS, and 3SD-NNS that differ in the number of parameters they share.[2] Since we transform the first neural network to always output 1, we set its filter parameters to zero and do not estimate them. Although not strictly necessary, we impose the same shared parameter structure on A as on B_γ for each model. In the static model, $\boldsymbol{\gamma}_t$ is constant and equals $\boldsymbol{\omega}_2$, with A as on B_γ set to zero. In 1SD-NNS, we assume a single learning rate per neural network and identical mean reversion speeds for weights and biases. In 2SD-NNS, we allow individual learning rates and mean-reversion speeds for the weights in the first layer of both neural networks, (w_{11}, w_{12}, w_{13}); the weights in the second layer of both networks, (w_{21}, w_{22}, w_{23}); and the first-layer biases of both networks, (b_1, b_2, b_3). In 3SD-NNS, all weights and biases of both neural networks are assigned individual learning rates and mean reversion parameters.

Finally, we use two scaling methods: identity scaling and scaling using the EWMA approach given in (16)–(17). In the model names, these are denoted by SD (identity) and SSD (EWMA), such that 1SD-NNS refers to the first method and 1SSD-NNS to the second.

[2]The model implementations are available at https://github.com/Sicco123/YieldFactorModels.jl.

TABLE 2: Diagonal specification of A and B_γ

model	A and B_γ	# of parameters
NNS	$\mathbf{0}_{27\times 27}$	18
1SD-NNS, 1SSD-NNS	$\text{diag}\big(\mathbf{0}_9', s_1\mathbf{1}_9', s_2\mathbf{1}_9'\big)$	22
2SD-NNS, 2SSD-NNS	$\text{diag}\big(\mathbf{0}_9', (s_1, s_2, s_3)' \otimes \mathbf{1}_3', (s_4, s_5, s_6)' \otimes \mathbf{1}_3'\big)$	30
3SD-NNS, 3SSD-NNS	$\text{diag}\big(\mathbf{0}_9', (s_1, s_2, \ldots, s_9), (s_{10}, s_{11}, \ldots, s_{18})\big)$	54

2.6.1 Benchmark models

We benchmark our models against the random walk forecast and several yield curve models that are widely used in the literature. The standard Nelson–Siegel (NS) model follows Diebold and Li (2006). The dynamic Nelson–Siegel (DNS) variant of Diebold et al. (2005) keeps the loading matrix with exponential basis functions as given in (4), but lets the latent factors be governed by a Gaussian VAR(p) process, leading to a linear state-space model estimated using the Kalman filter. Koopman et al. (2010) extend the DNS model by treating the decay parameter λ as an additional state, and estimate the parameters using the extended Kalman filter. We refer to this nonlinear state space model as the TV-λ DNS.

Additionally, we propose a new model specification that naturally arises when combining the Nelson-Siegel model with our proposed filtering method from Section 2.4. We keep the Nelson–Siegel basis functions and allow its loading parameter λ to change over time. The recursion steps are the same as in the neural network version, but the loading matrix is replaced by the Nelson–Siegel basis functions. We refer to this model as SD-NS when paired with unit scaling (i.e. S_t equal to the identity matrix) and as SSD-NS for the version with EWMA scaling as in (16)–(17). Lastly, in the search for the best forecasting model, we include three equally weighted ensembles that each include two models: the Static Ensemble, the SD Ensemble, and the SSD Ensemble. We use equal-weight ensembles because they often outperform more sophisticated weighting schemes (Timmermann, 2006). The Static Ensemble combines the NS and the NNS models. The SD Ensemble combines the SD-NS and the 1SD-NNS models. The SSD Ensemble combines the SSD-NS and the 3SSD-NNS models.

3 Simulation study

To guide our understanding of the capabilities and limitations of the introduced algorithm, we conduct a simulation study. The purpose is twofold. First, the simulations illustrate the differences between models with static factor loadings and models with time-varying loadings. Second, they allow us to assess how neural networks compare to Nelson-Siegel specification. The design of the data generating process combines an empirically calibrated static Nelson-Siegel model with deterministically imposed time-variation, which lets us study these differences in a realistic environment. We note that as a result, all models are mis-specified.

We generate yields from a dynamic three-factor Nelson-Siegel model,

$$\boldsymbol{y}_t = \Gamma^{NS}(\boldsymbol{\tau}; \lambda_t)\, \boldsymbol{\beta}_t + \boldsymbol{\varepsilon}_t, \qquad \boldsymbol{\varepsilon}_t \sim \mathcal{N}(\mathbf{0},\, \Sigma_\varepsilon),$$

where the loading functions $\Gamma^{NS}(\boldsymbol{\tau}; \cdot)$ are specified as in Remark 2.1. The factors follow a VAR(1),

$$\boldsymbol{\beta}_t = \boldsymbol{\omega} + B\, \boldsymbol{\beta}_{t-1} + \boldsymbol{u}_t, \qquad \boldsymbol{u}_t \sim \mathcal{N}(\mathbf{0},\, \Sigma_u),$$

with

$$\boldsymbol{\omega} = \begin{bmatrix} 5.64 \\ -2.42 \\ -1.27 \end{bmatrix}, \quad B = \begin{bmatrix} 0.99 & 0.00 & 0.00 \\ 0.00 & 0.95 & 0.00 \\ 0.00 & 0.00 & 0.93 \end{bmatrix}, \quad \Sigma_u = \begin{bmatrix} 0.15 & -0.11 & -0.01 \\ -0.11 & 0.14 & 0.02 \\ -0.01 & 0.02 & 0.66 \end{bmatrix}, \quad \Sigma_\varepsilon = 0.07 I_N.$$

All parameters are empirically calibrated by estimating a Nelson-Siegel model with static loadings and a static λ on U.S. Treasury yield data from January 1985 to December 2024. The values shown are rounded for clarity, but the simulations use the unrounded estimates. For numerical stability, we assume a diagonal B matrix in the simulations. The yields and factors are generated through the random components $\boldsymbol{\varepsilon}_t$ and $\boldsymbol{u}_t$.

Finally, the sequence λ_t is specified by one of the following: an AR(1) process, structural breaks or an empirically estimated path.

Empirically estimated: We use the empirical estimates of λ_t from the SSD-NS model as a deterministic path in our simulations. Originally, we have 480 monthly estimates based on our empirical sample. We increase the number of observations by repeating the sequence more than once. To smooth out any large jumps at the concatenation point, we linearly interpolate between the start and the tail of the path. We consider this specification as the most realistic of the three.

AR(1): For this specification, we generate an auxiliary variable,

$$a_t = 0.99a_{t-1} + \delta_t, \qquad \delta_t \sim \mathcal{N}(0, 0.01),$$

and then transform it so that it is positive, and matches the mean (0.07) and standard deviation of the SSD-NS estimates of λ_t. The resulting paths display high persistence with smooth time-variation. Moreover, the paths are random, so each simulation repetition features a unique path, allowing the models to be evaluated across different circumstances.

Structural breaks: Additionally, we test the models' ability to capture abrupt time-variation, we let λ_t cycle deterministically between $0.03, 0.07, 0.2$, and 0.07 in intervals of length 24. The values 0.03 and 0.2 approximate the lower and upper bounds of the estimated λ_t from our empirical data, while 0.07 represents a moderate level. In contrast to the autoregressive case, this process is fully deterministic.

We simulate yields for 24 maturities, 1-12, 18, 24, 30, 36, 48, 60, 72, 84, 96, 108, 120, 180 months, using sample sizes of 250, 500, and 2000 of in-sample observations. In each case, we simulate 500 additional observations to assess out-of-sample performance. We use the same selection of maturities as in the empirical application. The simulation experiment is replicated 500 times.

For each replication, we estimate the NS, NNS, SD-NS, SSD-NS, and 1SSD-NNS models. This simulation study is designed to show that the neural network models can compete with the Nelson–Siegel models even when the true factor loadings are generated using Nelson–Siegel functions, i.e., when the NS model is least mis-specified. Since adding more models would add little value, we only include two versions of the SDNFMs (NNS and 1SSD-NNS) to avoid unnecessary computational cost.

All models produce one-month and twelve-month-ahead forecasts for all maturities. To evaluate forecast accuracy, we report relative root mean squared error (RRMSE) defined relative to a random walk (RW) model. Table 3 shows the RRMSEs averaged over repetitions and over all maturities except the 180-month maturity, which is included as an anchoring point, for all sample sizes and all time-variation specifications.

TABLE 3: RRMSE Averaged over Maturities w.r.t. RW for forecast horizons 1 and 12 (500 simulations)

	Horizon 1			**Horizon 12**		
Model	250	500	2000	250	500	2000
AR(1)						
RW	1.000	1.000	1.000	1.000	1.000	1.000
NS	1.003	0.981	0.974	1.102	1.005	0.968
NNS	1.008	0.982	0.973	1.098	0.988	0.944
SD-NS	1.013	0.978	0.970	1.140	1.006	0.966
SSD-NS	1.009	0.977	0.970	1.129	1.005	0.966
1SSD-NNS	1.017	0.980	0.968	1.141	1.002	0.946
Structural Breaks						
RW	1.000	1.000	1.000	1.000	1.000	1.000
NS	1.007	0.990	0.984	1.079	0.995	0.965
NNS	1.008	0.989	0.982	1.057	0.975	0.939
SD-NS	658.592	0.988	0.975	1972.743	1.010	0.957
SSD-NS	1.007	0.980	0.974	1.107	0.993	0.955
1SSD-NNS	1.012	0.982	0.972	1.095	0.986	0.937
Empirically Estimated						
RW	1.000	1.000	1.000	1.000	1.000	1.000
NS	0.996	0.976	0.972	1.090	1.003	0.971
NNS	0.998	0.975	0.969	1.067	0.972	0.940
SD-NS	1.446	0.975	0.969	2.044	1.000	0.968
SSD-NS	1.001	0.974	0.969	1.110	1.000	0.968
1SSD-NNS	1.006	0.975	0.967	1.097	0.983	0.942

For the one-step-ahead forecasts and the smallest sample size, the simplest model, NS, per-

forms better than the other proposed models across all three simulation designs. Its parsimony avoids it from overfitting, although the neural network, which has 17 more parameters, performs almost as well. Under the strongest time-variation, the structural breaks, the SSD-NS model already matches the performance of NS, while SD-NS fails to generalize out-of-sample. Its gradient updates are occasionally very large, producing factor loading matrices that fit the data poorly. The model then takes time to recover, during which forecast errors accumulate.

For the medium sample size, the self-driving models begin to dominate. All three time-varying alternatives outperform their static counterparts. SSD-NS yields the lowest forecast errors across all data generating processes. Interestingly, NNS starts to outperform NS by a small margin, whereas 1SSD-NNS does not yet improve on SSD-NS. The 1SSD-NNS specification appears to require either more data or a stronger time-variation signal, whereas the parsimony of SSD-NS helps in shorter samples.

For the largest sample size, NNS fits the data better than NS in all experiments, even though the true factor loadings have the Nelson-Siegel shape. This improvement extends to 1SSD-NNS, which outperforms all NS-based competitors. The gains from allowing time-variation remain largest for the structural-break design and smallest for the empirically estimated case.

For the twelve-month-ahead forecasts, the results differ from those at the one-month-ahead horizon. For the smallest sample size, the NNS models have the lowest relative forecast errors among the estimated models, although all models perform worse than the RW. This reflects the accumulation of estimation error in the recursive forecasting scheme. With only a short sample, the parameter estimates are less stable, and the resulting estimation error propagates and amplifies as the forecast horizon increases. For the largest sample size, NNS and 1SSD-NNS consistently outperform RW with similar RRMSEs that are lower than for the rest of the models. The ranking between NNS and 1SSD-NNS depends on the specification with NNS slightly outperforming 1SSD-NNS for the AR(1) and 'Empirically Estimated' scenarios while 1SSD-NNS outperforms against 'Structural Breaks'. Medium-sized datasets show intermediate

results with good performance at close forecast horizons, that deteriorates as the forecast horizon increases. The accuracy of long-term forecasts, therefore, depends on the amount of data available for the estimation of the models.

We also investigate the role of scaling. SSD-NS consistently outperforms SD-NS for smaller samples, but the difference largely disappears for the largest sample. Without scaling, large errors can occasionally produce unrealistically large gradients. These exploding gradients make the subsequent forecast even worse, after which the model typically returns to normal. Figure 1 shows the λ_t forecasts of SSD-NS and SD-NS. The wider confidence bands for SD-NS reflect these episodes. Spikes appear in both the upward and downward directions, although they are more visible upward due to the positivity restriction on λ_t. Note that the estimates tend not to reach the value 0.2 in the high regime and instead on average only reach approximately 0.13. The mean reversion keeps the estimates from reaching larger values. The models favor underestimating λ_t in the high regime, which allows them to return to the moderate regime more quickly and leads to lower mean squared error.

For larger sample sizes, the λ_t forecasts become smoother and the two models behave more similarly. However, even with large samples, scaling remains advisable in empirical applications. In our simulations, the time-variation is repetitive and predictable, whereas real data may generate previously unseen patterns or large unprecedented shocks. Scaling makes the model more robust to such anomalies.

Finally, it is important to emphasize that the empirical λ_t paths used to inform our simulation data generating process represent a delayed and dampened projection of the true time-variation. Even when the empirical estimates show substantial movements, they can only react with a lag to the underlying variations, and they inevitably smooth out part of the true dynamics. This dampening is also visible in Figure 1 and illustrate how these models gradually adapt and lag behind when the underlying changes move more quickly than the model can accommodate. The actual data generating process for the yield curve is unknown and may

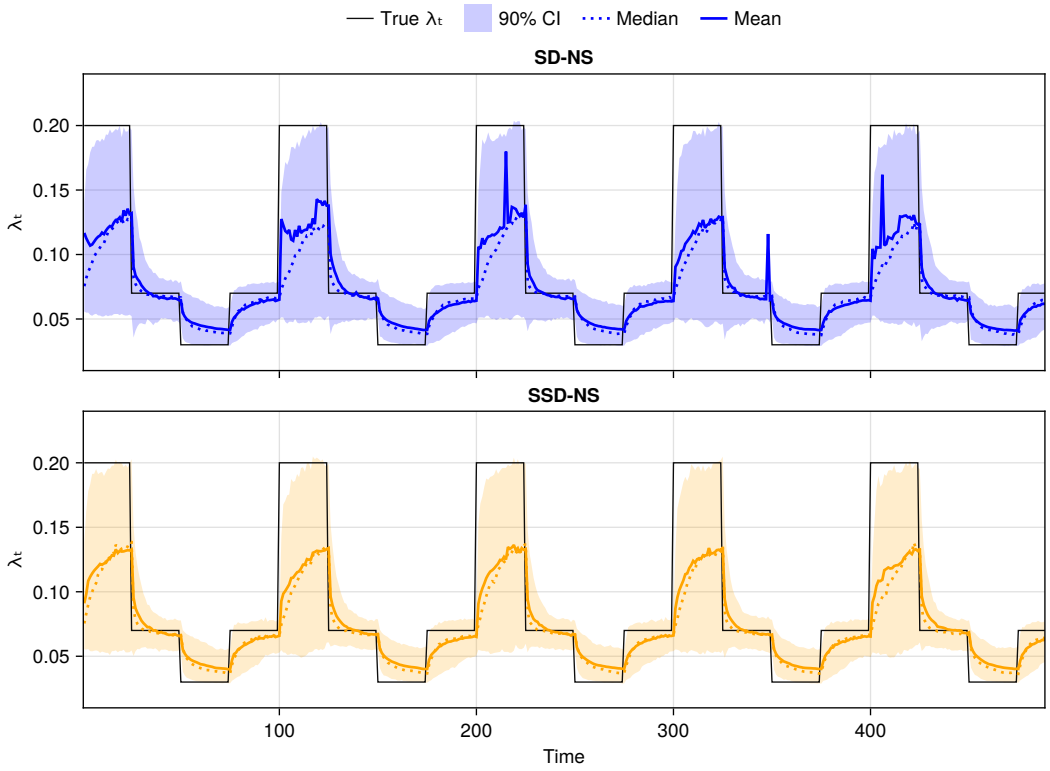

FIGURE 1: Average, median, 10% quantile, and 90% quantile of estimated λ_t for step-function λ_t paths.

involve richer, more abrupt, or more transient forms of time-variation than those captured by our estimation. In empirical settings, the time-variation may therefore be faster and stronger. This implies that the potential benefits of allowing time-varying factor loadings could be even larger in practice than what is suggested by the simulation designs.

4 Empirical Study

4.1 Data and empirical set-up

We use monthly zero-coupon yields on U.S. Treasury securities from the dataset of Liu and Wu (2021). The yields are constructed with a non-parametric kernel-smoothing method that retains more information from the raw yield data and delivers smaller pricing errors than competing methods. The full panel spans maturities from one month to thirty years and begins in 1961.

Observations from January 1985 to February 2004 serve as the training sample, and those

from March 2004 to December 2024 form the test set. A subset of the maturities is displayed in Figure 2. Because changes in monetary policy have influenced yield curve dynamics, we begin the training sample at the start of the Great Moderation, when the Federal Reserve committed to low and stable inflation. We use the yields with the following maturities: 1-12, 18, 24, 30, 36, 48, 60, 72, 84, 96, 108, 120, and 180. We include more of the shorter maturities because they contain most of the information about the shape of the yield curve. Table 1 implies that the factor loadings for the first and last maturities are anchored. While our main interest is in the yield curve up to 10 years, we include the 180-month maturity so that the anchoring is applied at 180 months rather than at 120 months, which allows the model to remain more flexible at the 120-month maturity. For forecasting, we assess model performance at maturities 3, 6, 12, 24, 60, and 120 to provide a clear overview and to ensure the results are not driven solely by the shorter maturities. The choice of the maturities is standard in the literature and relevant for different groups of stakeholders, e.g., households, businesses, or central banks. The results for all 24 maturities are reported in the appendix. With the current selection of maturities, the model is not designed to forecast the 180-month maturity. If that maturity is of interest, we recommend adding more data on longer maturities and reducing the emphasis on shorter ones.

Our goal is to forecast these yields at horizons one to twelve months ahead. We compare several variants of the SD-NNS model with the benchmarks. To find the best forecasting model, we also consider three ensemble specifications as explained earlier: the Static Ensemble, combining NS and NNS; the SD Ensemble, combining SD-NS and 1SD-NNS; and the SSD Ensemble, combining SSD-NS and 3SSD-NNS. All models are re-estimated recursively with a moving window, and out-of-sample performance is evaluated using the root mean squared error (RMSE).

Practitioners may be interested in different parts of the yield curve at different forecast horizons. To compare forecasts for a specific maturity and horizon, we assess statistical significance

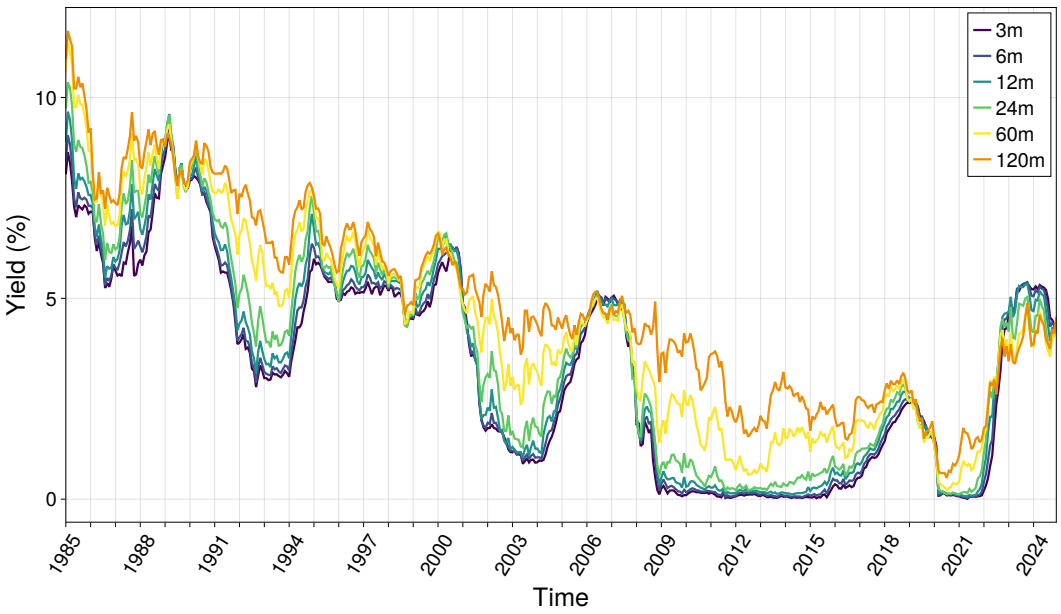

FIGURE 2: Yields over time for the 3, 6, 12, 24, 60 and 120 months

using the Diebold-Mariano test adjusted for multi-step horizons, as described in Harvey et al. (1997). Alternatively, one may wish to compare models at a given maturity irrespective of the forecast horizon. Therefore, we use the multi-horizon forecast comparison test for superior predictive ability (SPA) proposed by Quaedvlieg (2021), which allows to compare performance across all horizons of interest simultaneously. The test has two variants: uniform SPA (uSPA), which evaluates superior performance at each individual horizon, and average SPA (aSPA), which allows inferior performance at some horizons to be compensated by superior performance at others.

Lastly, one may also be interested in comparing models across maturities at a given horizon. Noting the similarity between the multi-horizon and multi-maturity data, the multi-horizon test can be directly applied in the maturity dimension instead of the horizon dimension. For all three levels of comparison, we evaluate multiple models by their squared error loss. For the Diebold-Mariano test we compare relative to the RW. For the SPA tests, we apply the model confidence set procedure of Hansen et al. (2011). The MCS is the set of models for which there is no significant evidence to differentiate them in terms of the chosen test statistic. Quaedvlieg

(2021) describe how both versions of the SPA test statistic can be used to construct model confidence sets.

4.2 Out-of-sample forecast results

4.2.1 Pairwise forecast comparison

Table 4 shows the 1-step-ahead out-of-sample relative RMSE for the random walk benchmark, two static factor models, six self-driving models, two of which are of the Nelson-Siegel type and four specifications of our neural factor models, two Kalman filter benchmarks, and three ensembles. The RMSE of each model is divided by that of the random walk. The first six columns present results for maturities of 3, 6, 12, 24, 60, and 120 months, and the column labeled "Average" shows the square root of the averaged squared errors across these maturities relative to the random walk. Stars indicate the rejection levels of the null hypothesis of equal MSEs.

TABLE 4: US Yield Curve Forecasting, Out-of-Sample Relative RMSE (Model RMSE / RW RMSE) for 1-Month-Ahead Forecast Horizon - Rolling Window

Model	m-3	m-6	m-12	m-24	m-60	m-120	Average
Benchmark							
RW	1.000	1.000	1.000	1.000	1.000	1.000	1.000
Static							
NS	0.900**	0.966	1.060	1.035**	1.065**	0.989	1.010
NNS	0.940	0.946	1.044	1.032	1.063**	1.029	1.018
Self-driving							
SD-NS	0.924**	0.928*	0.959	1.023	1.055*	0.992	0.991
SSD-NS	0.918***	0.927*	0.960	1.022	1.054*	0.984	0.988*
1SD-NNS	0.932*	0.961	0.982	1.024	1.054	0.980	0.996
1SSD-NNS	0.914**	0.949*	0.983	1.027	0.990	1.004	0.984**
2SSD-NNS	0.922**	0.964	0.962*	1.014	1.011	0.995	0.984**
3SSD-NNS	0.911**	0.933**	0.954**	1.018	1.018	0.993	0.980**
Kalman filter							
DNS	0.933	0.945	1.049	1.037**	1.076**	0.988	1.013
TVλ-DNS	0.962	0.914**	1.024	1.073***	1.042	1.001	1.011
Ensembles							
Static Ensemble	0.913**	0.948	1.049	1.029*	1.061*	0.999	1.008
SD Ensemble	0.907***	0.915***	0.955*	1.018	1.042	0.975	0.979**
SSD Ensemble	0.897***	0.903***	0.943**	1.017	1.023	0.979	0.971***

Notes: Asterisks denote Diebold–Mariano rejection of equal RMSE with the RW benchmark at *10%, **5%, and ***1% significance levels.

The static models perform worse on average than the random walk, with particularly poor performance at the 60-month maturity. All self-driving models improve on their static counterparts across all maturities, and the scaled versions further enhance performance. Among the self-driving specifications, the 3SSD-NNS delivers the lowest forecast errors, highlighting the added value of flexible factor loading structures. For the Kalman filter models, the DNS model behaves much like the static models, as expected. The TVλ-DNS model shows mixed performance, with notably low forecast error at the 6-month maturity but high error at 24 months. Turning to the ensembles, the self-driving ensembles in particular improve on the individual models they combine and achieve the largest gains at the shorter maturities.

TABLE 5: US Yield Curve Forecasting, Out-of-Sample Relative RMSE (Model RMSE / RW RMSE) for 12-Month-Ahead Forecast Horizon - Rolling Window

Model	m-3	m-6	m-12	m-24	m-60	m-120	Average
Benchmark							
RW	1.000	1.000	1.000	1.000	1.000	1.000	1.000
Static							
NS	0.866	0.893	0.935	1.027	1.092	1.032	0.952
NNS	0.872	0.883	0.902	0.949	0.980	0.982	0.914**
Self-driving							
SD-NS	0.865	0.891	0.936	1.037	1.145	1.058	0.962
SSD-NS	0.863	0.888	0.932	1.03	1.136	1.057	0.958
1SD-NNS	0.878	0.898	0.921	0.956	0.966	0.961	0.920*
1SSD-NNS	0.868	0.890	0.917	0.950	0.956	0.963	0.913**
2SSD-NNS	0.869	0.890	0.913	0.949	0.961	0.959	0.913**
3SSD-NNS	0.858	0.880	0.905	0.943	0.956	0.960	0.905**
Kalman filter							
DNS	0.850	0.871	0.909	0.983	1.072	1.043	0.930*
TVλ-DNS	0.850**	0.886*	0.938	1.013	1.128	1.128	0.958*
Ensembles							
Static Ensemble	0.862	0.881	0.909	0.969	1.005	0.965	0.917*
SD Ensemble	0.856	0.881	0.916	0.979	1.015	0.953	0.920*
SSD Ensemble	0.844	0.870	0.907	0.970	1.008	0.953	0.910**

Notes: Asterisks denote Diebold–Mariano rejection of equal RMSE with the RW benchmark at *10%, **5%, and ***1% significance levels.

Table 5 reports the 12-step-ahead out-of-sample relative RMSE. All models show improved relative performance compared to the random walk at the shorter maturities (3, 6, and 12 months). For the longer maturities (24, 60, and 120 months), the results are mixed. Only

the neural factor models produce lower forecast errors than the random walk across all six maturities. Consistent with the 1-month-ahead forecasts, the 3SSD-NNS delivers the lowest average forecast errors among the self-driving models. In contrast to the 1-month-ahead results, the SSD Ensemble now has higher average forecast error than the 3SSD-NNS, as the benefits of ensembling do not offset the weak performance of the NS models at the 60-month maturity. Lastly, a further difference between the 1- and 12-month-ahead horizons is that the benefit of adaptive factor loadings diminishes at longer horizons. The performance gap between the NNS and self-driving NNS models narrows, and for the NS models, the time-varying specifications often perform worse.

4.2.2 Multi-horizon forecast comparison

We show the model confidence sets of the aSPA and the uSPA multi-horizon forecast statistics and their associated p-values in Figure 3a and 3b respectively. We use the the forecast horizons of 1 up until 12 months and we use model confidence significance level, α_{MCS}, equal to 10%. A p-value lower than α_{MCS} indicates exclusion from the MCS. For each maturity, we indicate the models included in the MCS with a green (darker) color. Each maturity column corresponds to a new model confidence set.

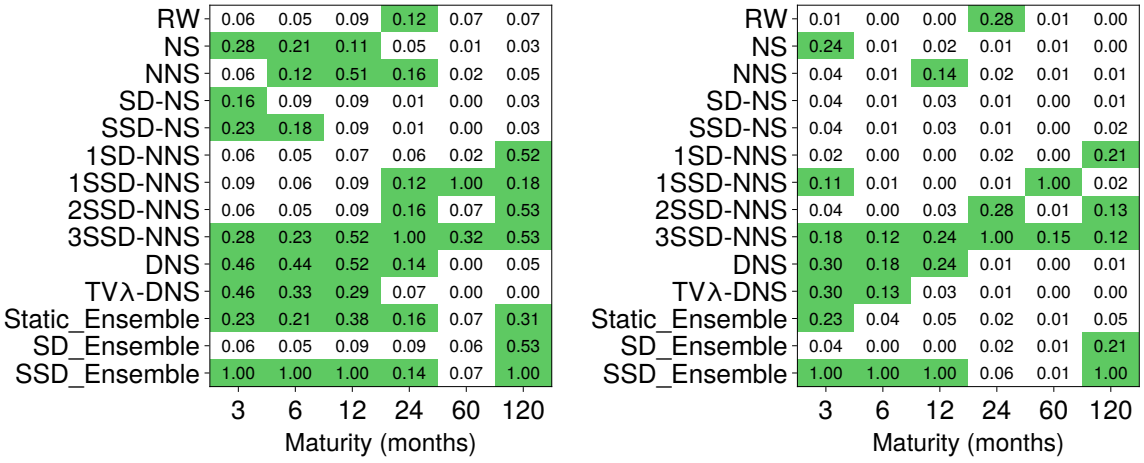

(a) aSPA (b) uSPA

FIGURE 3: MCS and p-values per maturity at significance level $\alpha_{MCS} = 0.1$ for $B = 999$ bootstrap samples

The 3SSD-NNS is not excluded from the MCS at any maturity under either the aSPA or uSPA versions of the test. It performs most distinctively at the 60-month maturity, where the MCS for both aSPA and uSPA consists only of the 1SSD-NNS and the 3SSD-NNS, with all other models excluded. While the 1SSD-NNS is excluded from the MCS at the lower maturities, the 3SSD-NNS is not. These findings confirm that the 3SSD-NNS is a consistently strong model across all maturities with most of its comparative advantage at the medium to medium-long maturities, the maturities shaping the curvature of the yield curve. Although many competing models provide comparable forecasts for the level and slope of the yield curve, they do not capture the curvature as well as the 3SSD-NNS. We further discuss how the curvature factor loadings of the 3SSD-NNS contribute to these results in Section 4.4.

Additionally, we see that as the complexity of our self-driving models decreases—e.g., going from 3SSD-NNS to 2SSD-NNS—the performance remains strong for medium and long-term maturities. This is in contrast with simpler approaches that tend to perform better only at short maturities and do not improve elsewhere on the yield curve as their complexity is increased.

4.2.3 Multi-maturity forecast comparison

Figure 4 presents the model confidence sets of the aSPA, Figure 4a, and the uSPA, Figure 4b, multi-maturity forecast statistics. We follow the same set-up as of the multi-horizon forecast comparison. For each horizon, we form MCSs based on the forecasts of the maturities: 3, 6, 12, 24, 60, 120.

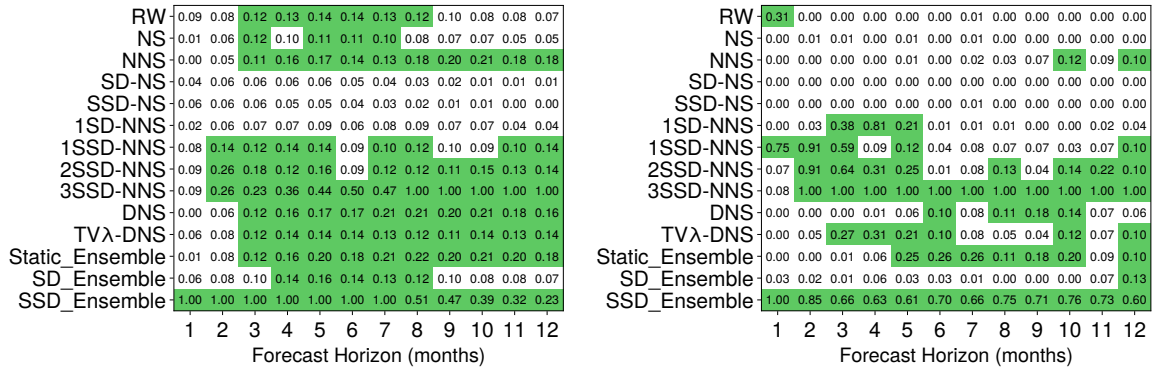

(a) aSPA

(b) uSPA

FIGURE 4: MCS and p-values per forecast horizon at significance level $\alpha_{MCS} = 0.1$ for $B = 999$ bootstrap samples

For both test statistics, the SSD Ensemble is always included in the model confidence set. The 3SSD-NNS is only excluded for the first forcast horizon for both tests. The 1-step-ahead forecast horizon Table 4 explains this. On average, the SSD Ensemble has lower forecast errors than the 3SSD-NNS, leading to its exclusion in the aSPA version of the test. The exclusion from the model confidence set at the first forecast horizon in the uSPA version of the test results from the SSD Ensemble having a much lower forecast error at the 6-month maturity, while 3SSD-NNS does not have significantly lower forecast errors than the SSD Ensemble at any maturity.

Summarizing these results, the 3SSD-NNS is consistently among the best-performing models, although the broader takeaway is that the SSD-NNS approach itself performs well. Across specifications, all SSD-NNS models deliver performance improvements that are not achieved by the competing models. The fact that 3SSD-NNS tends to outperform the other SSD-NNS versions mainly indicates that, as the complexity of the SSD-NNS specification increases, further gains in forecast accuracy can be achieved when sufficient data are available to support the additional flexibility.

Some modest improvement can still be obtained at the 1-month forecast horizon by using the ensemble of SSD-NS and 3SSD-NNS. Beyond that, certain models occasionally produce

lower forecast errors at specific maturities or horizons, but none exhibits significantly superior predictive ability across all maturities for a given horizon or across all horizons for a given maturity. This provides strong evidence in favor of using the SSD-NNS framework to forecast the U.S. yield curve.

4.3 Error accumulation over time

To better understand model performance and the evolution of RMSE over time, we analyze cumulative squared errors. Specifically, we compare the cumulative squared errors of the RW, NS, NNS, SSD-NS and 3SSD-NNS across short (3 months), medium (5 years), and long (10 years) maturities, for both 1-month and 12-month forecast horizons. Figure 5 displays these plots. Errors accumulate more quickly for the longer 12-month forecast horizon, as expected. Notably, significant increases in errors coincide with events like the Great Recession (late 2007 to mid-2009). During this period, 3SSD-NNS accumulates lower magnitude of errors than the other models for the short maturity. At the medium maturity, the random walk accumulates the least error, yet a gap remains between the 3SSD-NNS and the other models at the end of this period. At the long maturity, the NNS accumulates most of its error. The other models are close to each other. For the 12-month forecast horizon, especially the differences at the medium maturity are visible. The NS models perform much worse during this period. Other volatile periods are during early 2020 due to the COVID-19 epidemic and starting from 2022 due to the economic disruptions that emerged after the Russian invasion of Ukraine. These periods are also clearly visible in the forecasts of the yield curve in Figure 2.

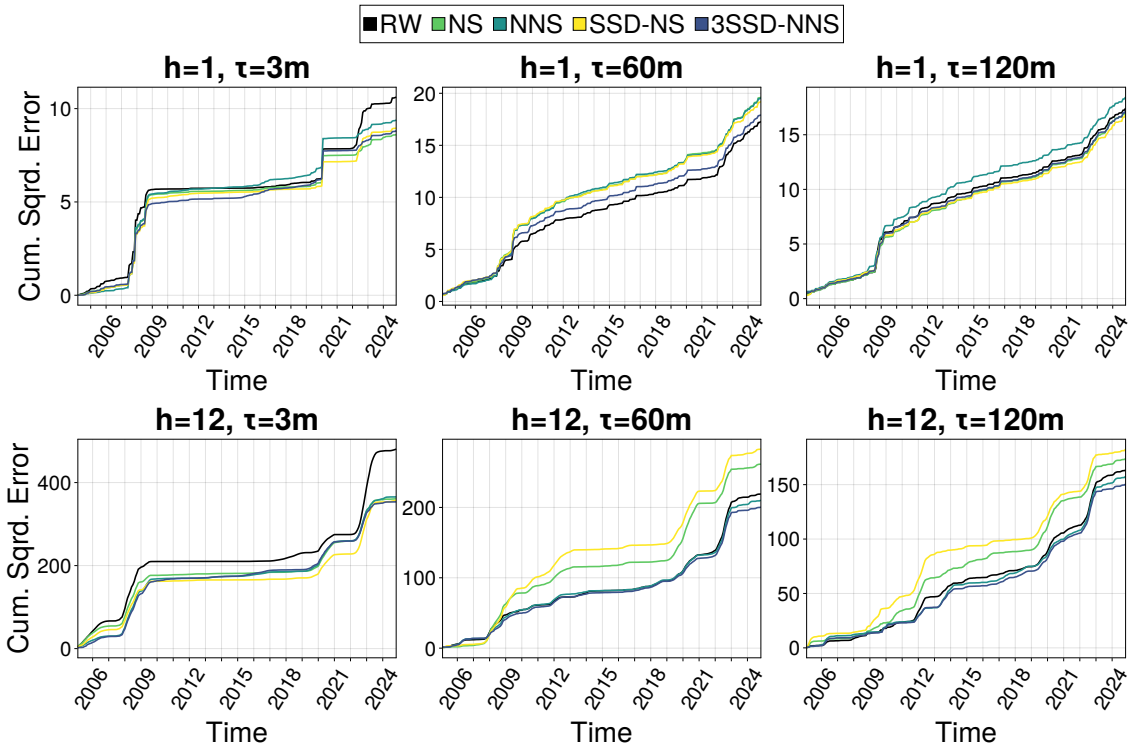

FIGURE 5: Comparison of cumulative error across forecast horizons (H) and maturities (τ): (a) H=1, τ =3; (b) H=12, τ =3; (c) H=1, τ =60; (d) H=12, τ =60; (e) H=1, τ =120; (f) H=12, τ =120.

4.4 In-sample analysis

Time-varying neural factor models consistently outperform Nelson-Siegel type models. The forecast comparison results show that, in particular at the medium and medium-long maturities, these time-varying neural factor models perform better than the Nelson-Siegel models. The differences between the models arise from their factor loadings and the factors they produce. The two classes of models differ in two main ways: the factor loading function and the specification of the dynamics in the factor loading parameters. The neural factor models use a neural network to generate the factor loadings instead of the Nelson-Siegel specification. The specification of the dynamics in the factor loading parameters also differs fundamentally: for the neural network, time-variation is governed by 18 time-varying parameters, whereas for SD-NS it is governed by a single time-varying parameter.

The out-of-sample forecast results show that both differences are important. At the long

forecast horizon, we see that the factor loading function of the neural network models leads to better forecast performance. The static NNS performs better than the NS model and the time-varying NS variants. At the short forecast horizon, it is especially the specification of the dynamics in the factor loading parameters that contributes to the lower forecast errors. At short forecast horizons, the time-varying NNS variants outperform the time-varying NS variants, whereas the static NNS model does not outperform the static NS model.

Motivated by these findings, we investigate in greater detail how the neural factor loadings and their time-varying parameters differ from the Nelson–Siegel specifications and how these differences contribute to the observed improvements in forecast performance. We estimate all models using the full sample from January 1985 to December 2024 and examine the resulting factor loadings and extracted factors.

4.5 Estimated Factor Loadings

We begin by comparing the static neural factor loadings to the static Nelson-Siegel loadings. We are primarily interested in the slope and curvature factor loadings since the level loadings are identical for both models. The estimated loadings are illustrated in Figure 6. The shapes of both loadings show similar patterns. The loading on the second factor decreases monotonically, and approaching zero as the maturity increases. The loading on the third factor initially increases sharply, reaching its maximum at the 30-month maturity for NNS model and 48-month maturity for NS model. After, reaching their maximum both decrease monotonically.

Partially, these shapes are directly imposed by each model's specific approximation method. Although neural networks offer greater flexibility in capturing shapes, their flexibility is constrained by their transformations. The Nelson-Siegel approximations are less flexible but do not anchor the loading for the shortest and longest maturity. The Nelson-Siegel model can assign more weight to the longest maturity where the transformed neural network cannot.

However, Figure 6 also highlights a limitation in interpreting the factors within the Nelson-

Siegel framework. The second and third factor load substantially on the longest-maturity yield, implying that part of the yield's level is absorbed by these factors. This overlap reduces the interpretability of the Nelson-Siegel first factor and, consequently, also of the second and third factors. By contrast, the explicit constraints imposed by the NNS transformations on the boundary neural factor loadings provide a clearer interpretation, as they ensure that the longest-maturity yield cannot load on the second and third factors and the shortest maturity cannot load on the third factor.

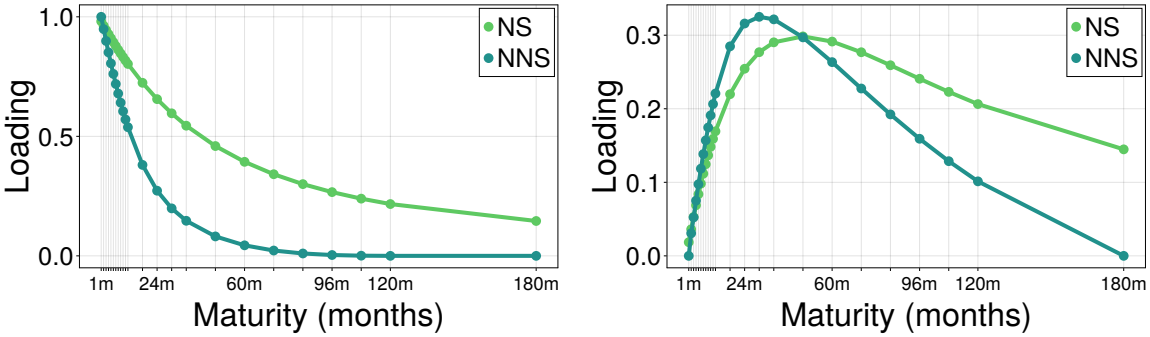

FIGURE 6: Estimated factor loadings curves for static models NNS and NS

In Figure 7, we show the time-varying paths of the one-step-ahead predicted factor loadings. Each line represents one entry in the factor loading matrix for a corresponding maturity. For the curvature factor loadings, we display only a subset of the maturities to improve readability. This comparison focuses on the 3SSD-NNS and SSD-NS models.

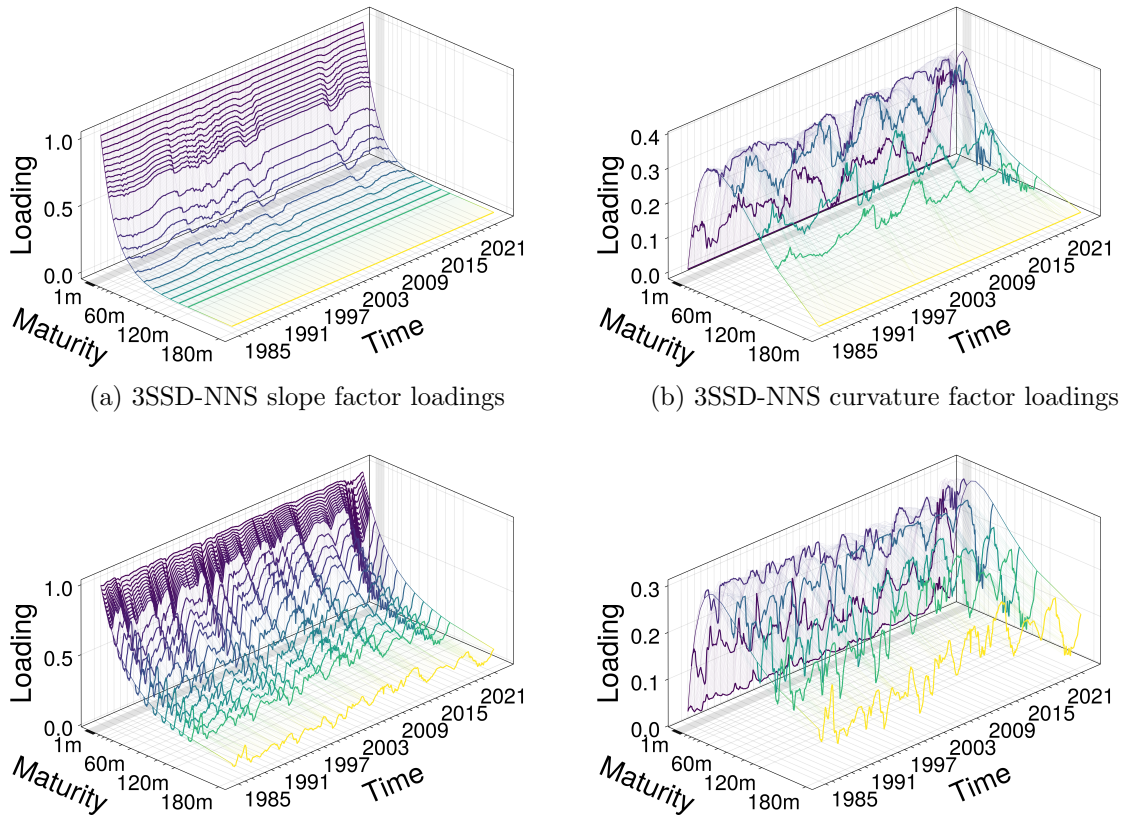

(a) 3SSD-NNS slope factor loadings

(b) 3SSD-NNS curvature factor loadings

(c) SSD-NS slope factor loadings

(d) SSD-NS curve factor loadings

FIGURE 7: Comparison of time-varying factor loadings

The SSD-NS loadings exhibit stronger time-varying behavior compared to the neural loadings. The SSD-NS loadings are unrealistically noisy, while the neural loadings capture more persistent trends. The nine time-varying parameters of the neural network are more robust at capturing time-variation than the single time-varying parameter of the Nelson-Siegel model. Additionally, the slope loadings of the 3SSD-NNS are more static than the curvature loadings. For the SSD-NS, a single parameter produces the time-variation in both factor loadings, so more time-variation in the curvature loadings also results in more time-variation in the slope loadings. The flexibility of allowing different speeds of adjustment to new information for the slope and curvature factor loadings contributes to better performance. When examining the slope factor loadings of the 3SSD-NNS, we observe that around the Great Recession and the COVID-19 epidemic the slope loadings place less weight on higher maturities and assign rel-

atively more weight to the lower maturities, while during the zero-lower-bound period higher maturities receive more of the slope loading.

To further understand the dynamics of the curvature loadings, Figure 8 shows the maturity with largest one-month-ahead curvature loading for every month and the shortest range between two maturities that covers at least 50% of the total curvature factor load. The loading mass moves around the 36-month into the direction where the curvature factor can explain most of the yield curve. March 1998 and December 1999 and February 2005 and October 2007 are both periods with relatively high loading on longer maturities which are followed by rapid movement toward loading on short maturities. These contribute to better capturing the inverted yield curve present at those times. Interestingly, between April 2022 and December 2024 there is also a period of an extended inverted yield curve, but here the curvature factor loads an unprecedented amount at the shorter maturities.

Additionally, we note that the range of maturities that have at least 50% loading on the curvature factor is evolving in time. There are periods of time where the curvature factor contributes to both a low and a high range of maturities. The symmetry of the span is also not constant with periods, e.g., 1991–1994 or after 2021 characterized by high degree of assymetry.

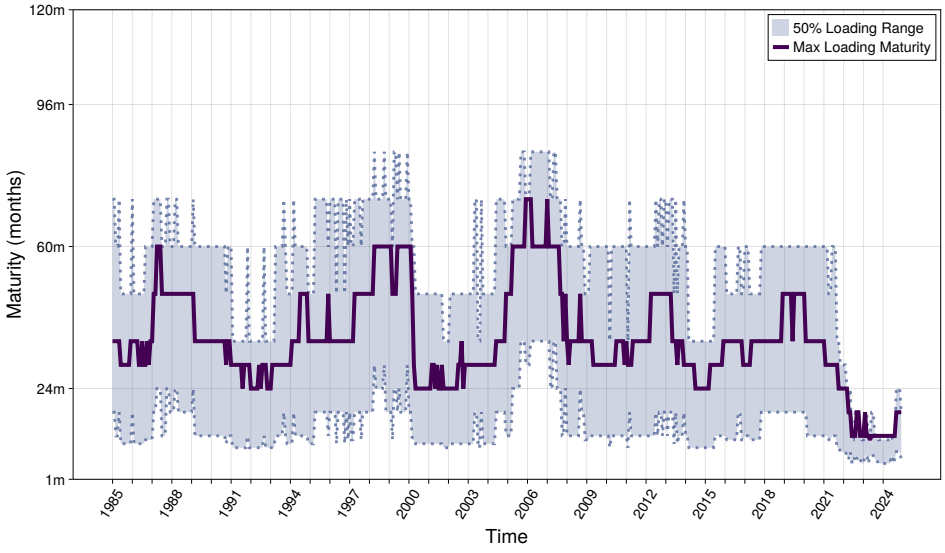

FIGURE 8: Curvature factor loading maximizing maturity and smallest 50% curvature factor loading coverage range.

4.6 Estimated Factors

In Figure 9, we compare the three predicted factors obtained with 3SSD-NNS and Nelson–Siegel (NS), and we plot their data-based proxies similar to Koopman et al. (2010). We proxy the level factor with the 180-month yield, the slope with the spread between the 1-month and 180-month yields, and the curvature with twice the 36-month yield minus the 3-month yield minus the 180-month yield. We choose the 36-month yield to represent curvature since it is where the 3SSD-NNS places the most curvature factor loading most of the time.

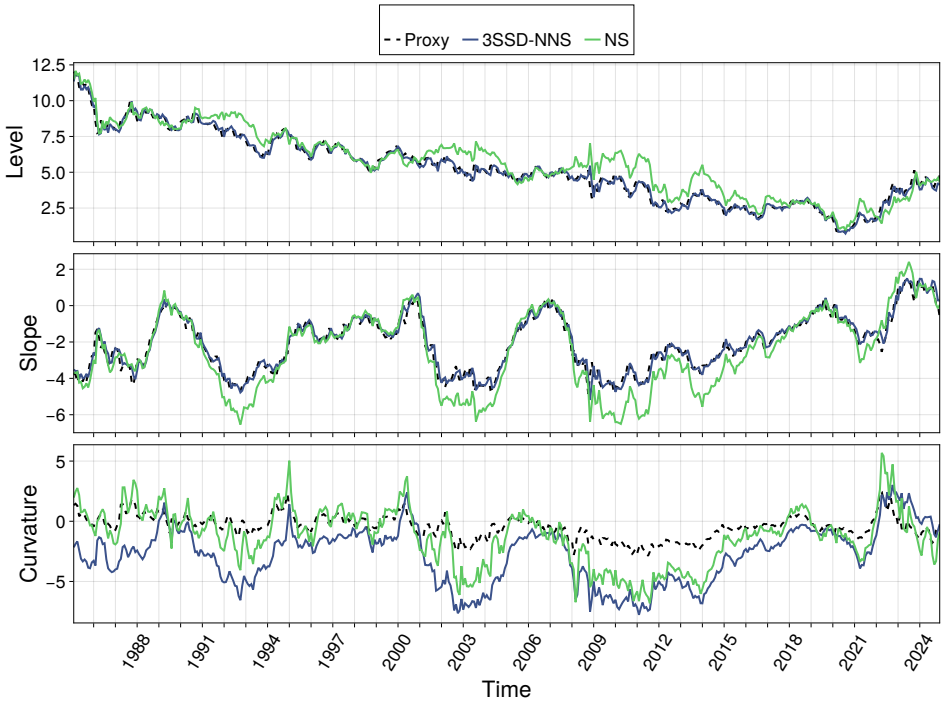

FIGURE 9: **Level, slope and curvature.** From top to bottom, the panels show the level, slope and curvature. The blue (dark) colored lines are the 1-step-ahead predicted factors of the 3SSD-NNS model; the green (light) colored lines are the NS benchmark predictions. The dashed lines represent level, slope and curvature proxies.

The neural factor model tracks the level and slope data proxies well throughout the sample, while Nelson-Siegel model does not. In particular, during 1991–1994, 2001–2005 and 2008–2016, the NS does not follow the slope and level data proxies while the neural model does. Interestingly, the NS model aligns more closely with the curvature proxy than the neural model. The curvature proxy does not align well with the neural model because the curvature data proxy

relies on the curvature peak to be at the 36-month maturity while the 3SSD-NNS let's the curvature peak vary over time. Letting the curvature peak change adaptively produces a more meaningful curvature factor than static versions.

4.7 Case study

Now that we know how the factor loadings and factors vary over time, we can go one step further by analyzing the resulting yield curve. We examine two dates where the forecast error is large and therefore we expect a relatively large update in the factor loadings. We are interested in how the 3SSD-NNS adapts to these large errors. Figure 10 and Figure 11 show a snapshot of the yield curve, the one-step-ahead predictions from one month earlier, the current one-step-ahead predictions, and the corresponding factor loadings.

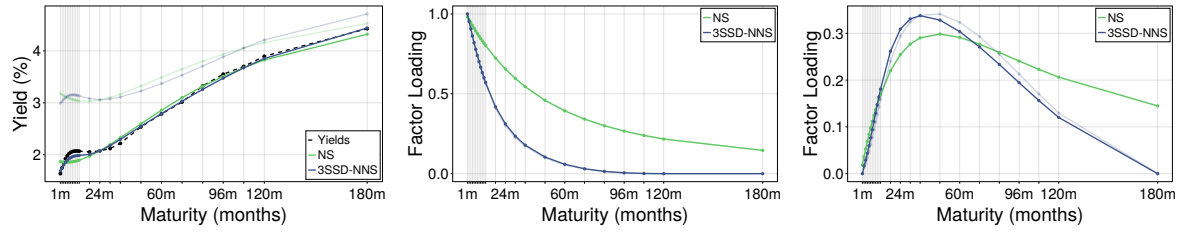

(a) Yield curve (b) Slope factor loadings (c) Curvature factor loadings

FIGURE 10: Snapshot yield curve January 2008, one-step-ahead predictions December 2007 (semi-transparent), one-step-ahead predictions January 2008 (opaque)

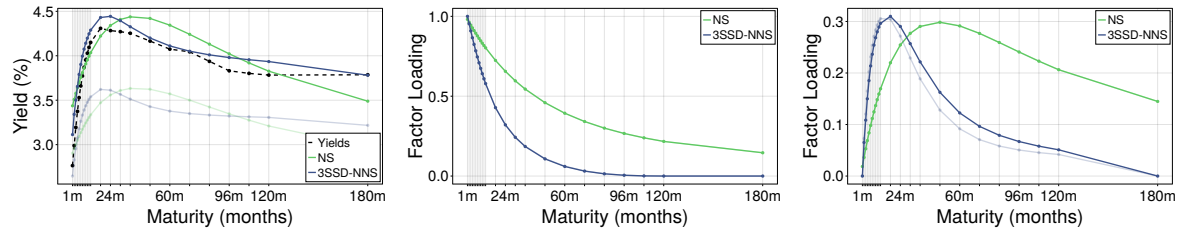

(a) Yield curve (b) Slope Factor Loadings (c) Curvature Factor Loadings

FIGURE 11: Snapshot yield curve September 2022, one-step-ahead predictions August 2022 (semi-transparent), one-step-ahead predictions September 2022 (opaque)

We are interested in how the yield curve's information is incorporated into the next predictions. In January 2008, we see that for both models there is a large shift in the slope of the yield

curve and a small shift in the level. The curvature moves in the direction of the shorter maturities, which is visible in the corresponding change in the curvature factor loadings. The update of the slope factor loadings of the 3SSD-NNS model are negligible. Interestingly, the observed yield curve starts with a concave-shaped segment, then becomes convex, and later becomes concave again. The NS model misses the first concave-shaped episode, while the 3SSD-NNS is able to capture it.

In September 2022, the yield curve has a very different shape where a large part of the curve is inverted, i.e., downward sloping. Again, there is a clear level shift. The curvature moves slightly toward the longer maturities. The shape of the curvature factor loadings is clearly reflected in the predictions. Although the model does not fit better than the NS model at some maturities, such as the 120-month maturity, it clearly provides a better fit at the medium to medium-long maturities in September 2022.

5 Conclusion

This paper introduces a novel framework for factor modeling with time-varying loadings, named the Self-Driving Neural Factor Model (SDNFM). The loading matrix and factors are recursively updated in the least squares direction at each time point to track variations in both. Filtered neural network parameters allow for adaptation to changing economic conditions, where static neural networks cannot.

We conduct a yield curve forecasting exercise to evaluate the practical validity of our method. We demonstrate its advantages over static models. Applied to U.S. government bond yields, the proposed SDNFM delivers significantly better out-of-sample predictive accuracy compared to the random walk, where well-known benchmarks do not.

A key contribution of this work is that despite using a neural network, the factors remain interpretable. By construction, we impose Neural Nelson–Siegel (NNS) identification restrictions so that the factors can be interpreted as level, slope, and curvature factors of the yield

curve. This NNS transformation ensures unique identification of the model and have a clear interpretation than factors of the Nelson–Siegel factors (Nelson and Siegel, 1987).

We demonstrate how SDNFM is effective in the well-established field of yield curve forecasting, where the factor structure is well understood and provides a natural benchmark. Beyond this specific application, SDNFM is a flexible and generalizable framework that can be extended to other multivariate forecasting problems. In particular, when there are variables or an observed structure that describe the relationship of the entries of the loading matrix, this can be flexibly tracked by the self-driving neural networks.

References

Avramov, D., Cheng, S., and Metzker, L. (2023). Machine Learning vs. Economic Restrictions: Evidence from Stock Return Predictability. *Management Science*, 69(5):2587–2619.

Bai, J. and Ng, S. (2013). Principal components estimation and identification of static factors. *Journal of Econometrics*, 176(1):18–29.

Bai, J. and Wang, P. (2015). Identification and Bayesian Estimation of Dynamic Factor Models. *Journal of Business and Economic Statistics*, 33(2):221–240.

Barigozzi, M. and Luciani, M. (2024). Quasi Maximum Likelihood Estimation and Inference of Large Approximate Dynamic Factor Models via the EM algorithm. *Finance and Economics Discussion Series*, (2024-086):1–135.

Bernanke, B., Boivin, J., and Eliasz, P. (2003). Measuring the Effects of Monetary Policy: A Factor-Augmented Vector Autoregressive (FAVAR) Approach. *Finance and Economics Discussion Series*, 2003.0(3):1–47.

Bianchi, D., Büchner, M., and Tamoni, A. (2021). Bond Risk Premiums with Machine Learning. *Review of Financial Studies*, 34(2):1046–1089.

Chen, L., Pelger, M., and Zhu, J. (2024). Deep Learning in Asset Pricing. *Management Science*, 70(2):714–750.

Cheung, Y. L. (2024). Identification of Time-Varying Factor Models. *Journal of Business and Economic Statistics*, 42(1):76–94.

Christensen, J. H., Diebold, F. X., and Rudebusch, G. D. (2011). The affine arbitrage-free class of Nelson-Siegel term structure models. *Journal of Econometrics*, 164(1):4–20.

Creal, D., Koopman, S. J., and Lucas, A. (2013). Generalized autoregressive score models with applications. *Journal of Applied Econometrics*, 28(5):777–795.

Creal, D., Koopman, S. J., Lucas, A., and Zamojski, M. (2024). Observation-driven filtering of time-varying parameters using moment conditions. *Journal of Econometrics*, 238(2).

Del Negro, M. and Otrok, C. (2008). Dynamic factor models with time-varying parameters: measuring changes in international business cycles. Technical Report 326, Federal Reserve Bank of New York.

Diebold, F. X. and Li, C. (2006). Forecasting the term structure of government bond yields. *Journal of Econometrics*, 130(2):337–364.

Diebold, F. X., Piazzesi, M., and Rudebusch, G. D. (2005). Modeling bond yields in finance and macroeconomics. *American Economic Review*, 95(2):415–420.

Doz, C., Giannone, D., and Reichlin, L. (2012). A quasi-maximum likelihood approach for large, approximate dynamic factor models. *Review of Economics and Statistics*, 94(4):1014–1024.

Gu, S., Kelly, B., and Xiu, D. (2020). Empirical Asset Pricing via Machine Learning. *Review of Financial Studies*, 33(5):2223–2273.

Gu, S., Kelly, B., and Xiu, D. (2021). Autoencoder asset pricing models. *Journal of Econometrics*, 222(1):429–450.

Hansen, P. R., Lunde, A., and Nason, J. M. (2011). The Model Confidence Set. *Econometrica*, 79(2):453–497.

Harvey, D., Leybourne, S., and Newbold, P. (1997). Testing the equality of prediction mean squared errors. *International Journal of Forecasting*, 13(2):281–291.

Jungbacker, B. and Koopman, S. J. (2015). Likelihood-based dynamic factor analysis for measurement and forecasting. *Econometrics Journal*, 18(2):C1–C21.

Kingma, D. P. and Ba, J. (2017). Adam: A method for stochastic optimization.

Koopman, S. J., Mallee, M. I., and Van Der Wel, M. (2010). Analyzing the term structure of interest rates using the dynamic Nelson-Siegel model with time-varying parameters. *Journal of Business and Economic Statistics*, 28(3):329–343.

Kose, M. A., Otrok, C., and Whiteman, C. H. (2003). International business cycles: World, region, and country-specific factors. *american economic review*, 93(4):1216–1239.

Liu, Y. and Wu, J. C. (2021). Reconstructing the yield curve. *Journal of Financial Economics*, 142(3):1395–1425.

Mikkelsen, J. G., Hillebrand, E., and Urga, G. (2019). Consistent estimation of time-varying loadings in high-dimensional factor models. *Journal of Econometrics*, 208(2):535–562.

Nelson, C. R. and Siegel, A. F. (1987). Parsimonious Modeling of Yield Curves. *The Journal of Business*, 60(4):473.

Quaedvlieg, R. (2021). Multi-Horizon Forecast Comparison. *Journal of Business and Economic Statistics*, 39(1):40–53.

Stock, J. H. and Watson, M. W. (2002). Forecasting using principal components from a large number of predictors. *Journal of the American Statistical Association*, 97(460):1167–1179.

Stock, J. H. and Watson, M. W. (2016). *Dynamic Factor Models, Factor-Augmented Vector Autoregressions, and Structural Vector Autoregressions in Macroeconomics*, volume 2. Elsevier B.V., 1 edition.

Su, L. and Wang, X. (2017). On time-varying factor models: Estimation and testing. *Journal of Econometrics*, 198(1):84–101.

Tieleman, T. and Hinton, G. (2012). Lecture 6.5 — "rmsprop: Divide the gradient by a running average of its recent magnitude". Coursera: Neural Networks for Machine Learning. Video lecture; section 6.5 of the course.

Timmermann, A. (2006). Chapter 4 forecast combinations. volume 1 of *Handbook of Economic Forecasting*, pages 135–196. Elsevier.

Zamojski, M. (2019). Self-driving score filters. Technical report.

A 24 maturities moving window

For completeness, we report the forecast evaluation results of the 23 maturities: 1 to 12, 18, 24, 30, 36, 48, 60, 72, 84, 96, 108, and 120 months. The models are the same as in Section 4, so they are not reestimated. The goal is to document that the conclusions in Section 4 are not a consequence of the smaller maturity set.

Table A1 reports the one-step-ahead relative RMSE for all maturities, while Table A2 shows the twelve-step-ahead results. Figure A1 presents the aSPA and uSPA model confidence sets across maturities for forecast horizons 1 to 12. Figure A2 shows the corresponding model confidence sets across the forecast horizons using all maturities.

The results remain very similar to those in the main text. The 3SSD-NNS continues to perform well across the entire curve and is rarely excluded from the model confidence set. Most competing models are excluded for large parts of the maturity range and for some of the horizons.

TABLE A1: US Yield Curve Forecasting, Out-of-Sample Relative RMSE (Model RMSE / RW RMSE) for 1-Month-Ahead Forecast Horizon - Moving Window

Model	m-1	m-2	m-3	m-4	m-5	m-6	m-7	m-8	m-9	m-10	m-11	m-12	m-18	m-24	m-30	m-36	m-48	m-60	m-72	m-84	m-96	m-108	m-120	Average
Benchmark																								
RW	1.000	1.000	1.000	1.000	1.000	1.000	1.000	1.000	1.000	1.000	1.000	1.000	1.000	1.000	1.000	1.000	1.000	1.000	1.000	1.000	1.000	1.000	1.000	1.000
Static																								
NS	0.935	0.907*	0.9**	0.913**	0.938*	0.966	0.993	1.015	1.034	1.048	1.056	1.06	1.036*	1.035**	1.052**	1.064**	1.074**	1.065**	1.052*	1.014	0.999	0.979	0.989	1.011
NNS	1.066	0.976	0.940	0.929**	0.934**	0.946	0.962	0.981	1.000	1.018	1.033	1.044	1.038	1.032	1.056*	1.078**	1.09**	1.063**	1.044*	1.001	0.987	0.977	1.029	1.017**
Self-driving																								
SD-NS	0.951	0.934*	0.924**	0.920***	0.923**	0.928*	0.933*	0.938	0.944	0.950	0.955	0.959	0.984	1.023	1.052*	1.063**	1.067*	1.055*	1.051*	1.021	1.015	0.996	0.992	0.993
SSD-NS	0.942	0.927**	0.918***	0.917***	0.921**	0.927*	0.933*	0.939	0.945	0.951	0.956	0.960	0.983	1.022	1.052*	1.063**	1.067*	1.054*	1.048	1.016	1.010	0.991	0.984	0.991
1SD-NNS	0.966	0.931	0.932*	0.943	0.954	0.961	0.963	0.964	0.967	0.971	0.976	0.982	1.002	1.024	1.041	1.051	1.069	1.054	1.04	1.005	0.993	0.967	0.980	0.996
1SSD-NNS	0.923**	0.914**	0.914**	0.927**	0.941*	0.949*	0.952*	0.954*	0.958	0.964	0.973	0.983	1.023	1.027	1.015	1.004	0.993	0.990	1.004	0.992	0.997	0.988	1.004	0.979***
2SSD-NNS	0.910**	0.911**	0.922**	0.941*	0.957	0.964	0.963	0.960*	0.957*	0.957*	0.958*	0.962*	0.989	1.014	1.023	1.026	1.021	1.011	1.018	1.000	0.997	0.981	0.995	0.982***
3SSD-NNS	0.919**	0.909**	0.911**	0.922**	0.931**	0.933**	0.933**	0.932**	0.933**	0.938**	0.946**	0.954**	0.997	1.018	1.022	1.023	1.023	1.018	1.025	1.004	0.999	0.980	0.993	0.977***
Kalman filter																								
DNS	1.023	0.968	0.933	0.92**	0.927**	0.945	0.967	0.990	1.011	1.028	1.041	1.049	1.04*	1.037**	1.049**	1.062**	1.080**	1.076**	1.067**	1.026	1.007	0.982	0.988	1.017**
TVλ-DNS	1.079	1.015	0.962	0.927	0.913**	0.914**	0.926**	0.945*	0.966	0.987	1.007	1.024	1.063***	1.073***	1.078**	1.073**	1.061*	1.042	1.046*	1.020	1.013	1.001	1.001	1.015**
Ensembles																								
Static Ensemble	0.990	0.932	0.913**	0.912***	0.927**	0.948	0.971	0.993	1.013	1.030	1.042	1.049	1.031	1.029*	1.050*	1.068**	1.079**	1.061*	1.045	1.005	0.989	0.972	0.999	1.009
SD Ensemble	0.926*	0.907**	0.907***	0.908***	0.912***	0.915***	0.919***	0.924**	0.931**	0.939**	0.947**	0.955*	0.986	1.018	1.040	1.048*	1.056	1.042	1.035	1.006	0.998	0.974	0.975	0.979***
SSD Ensemble	0.910**	0.897***	0.897***	0.899***	0.902***	0.903***	0.905***	0.909***	0.915***	0.924***	0.933**	0.943**	0.985	1.017	1.032	1.036	1.034	1.023	1.024	1.000	0.996	0.978	0.979	0.970***

Notes: Asterisks denote Diebold–Mariano rejection of equal RMSE with the RW benchmark at *10%, **5%, and ***1% significance levels.

TABLE A2: US Yield Curve Forecasting, Out-of-Sample Relative RMSE (Model RMSE / RW RMSE) for 12-Month-Ahead Forecast Horizon - Moving Window

Model	m-1	m-2	m-3	m-4	m-5	m-6	m-7	m-8	m-9	m-10	m-11	m-12	m-18	m-24	m-30	m-36	m-48	m-60	m-72	m-84	m-96	m-108	m-120	Average
Benchmark																								
RW	1.000	1.000	1.000	1.000	1.000	1.000	1.000	1.000	1.000	1.000	1.000	1.000	1.000	1.000	1.000	1.000	1.000	1.000	1.000	1.000	1.000	1.000	1.000	1.000
Static																								
NS	0.843	0.855	0.866	0.876	0.885	0.893	0.9	0.907	0.913	0.920	0.928	0.935	0.983	1.027	1.06	1.081	1.095	1.092	1.077	1.063	1.051	1.041	1.032	0.947**
NNS	0.872	0.867	0.872	0.877	0.88	0.883	0.886	0.888	0.891	0.894	0.898	0.902	0.928	0.949	0.966	0.976	0.984	0.98	0.979	0.977	0.974	0.974	0.982	0.911***
Self-driving																								
SD-NS	0.843	0.854	0.865	0.875	0.883	0.891	0.898	0.905	0.913	0.920	0.928	0.936	0.988	1.037	1.079	1.108	1.137	1.145	1.134	1.122	1.105	1.085	1.058	0.958*
SSD-NS	0.841	0.852	0.863	0.872	0.881	0.888	0.895	0.902	0.909	0.916	0.924	0.932	0.982	1.03	1.070	1.099	1.128	1.136	1.126	1.116	1.10	1.082	1.057	0.954**
1SD-NNS	0.863	0.868	0.878	0.886	0.893	0.898	0.903	0.906	0.910	0.913	0.917	0.921	0.943	0.956	0.964	0.967	0.968	0.966	0.968	0.968	0.965	0.962	0.961	0.918***
1SSD-NNS	0.852	0.858	0.868	0.876	0.884	0.890	0.895	0.900	0.904	0.908	0.913	0.917	0.939	0.95	0.955	0.956	0.957	0.956	0.96	0.965	0.964	0.963	0.963	0.910***
2SSD-NNS	0.850	0.858	0.869	0.878	0.885	0.890	0.895	0.899	0.902	0.906	0.909	0.913	0.935	0.949	0.958	0.962	0.964	0.961	0.962	0.963	0.960	0.958	0.959	0.910***
3SSD-NNS	0.844	0.847	0.858	0.867	0.874	0.880	0.885	0.889	0.893	0.897	0.901	0.905	0.929	0.943	0.953	0.957	0.958	0.956	0.959	0.961	0.959	0.958	0.960	0.902***
Kalman filter																								
DNS	0.833	0.841	0.85	0.857	0.865	0.871	0.877	0.883	0.889	0.896	0.902	0.909	0.949	0.983	1.010	1.031	1.058	1.072	1.076	1.073	1.065	1.056	1.043	0.926***
TVλ-DNS	0.819*	0.835**	0.85**	0.864**	0.876**	0.886*	0.896*	0.905*	0.914*	0.922*	0.930	0.938	0.980	1.013	1.041	1.066	1.106	1.128	1.142	1.145	1.143	1.141	1.128	0.953***
Ensembles																								
Static Ensemble	0.848	0.854	0.862	0.869	0.875	0.881	0.886	0.890	0.895	0.899	0.904	0.909	0.942	0.969	0.99	1.003	1.011	1.005	0.995	0.985	0.975	0.969	0.965	0.915***
SD Ensemble	0.836	0.845	0.856	0.866	0.874	0.881	0.887	0.893	0.899	0.904	0.910	0.916	0.952	0.979	1.0	1.012	1.019	1.015	1.006	0.997	0.983	0.970	0.953	0.917***
SSD Ensemble	0.823	0.833	0.844	0.854	0.863	0.870	0.877	0.883	0.889	0.895	0.901	0.907	0.942	0.97	0.991	1.003	1.011	1.008	1.000	0.992	0.980	0.968	0.953	0.907***

Notes: Asterisks denote Diebold–Mariano rejection of equal RMSE with the RW benchmark at *10%, **5%, and ***1% significance levels.

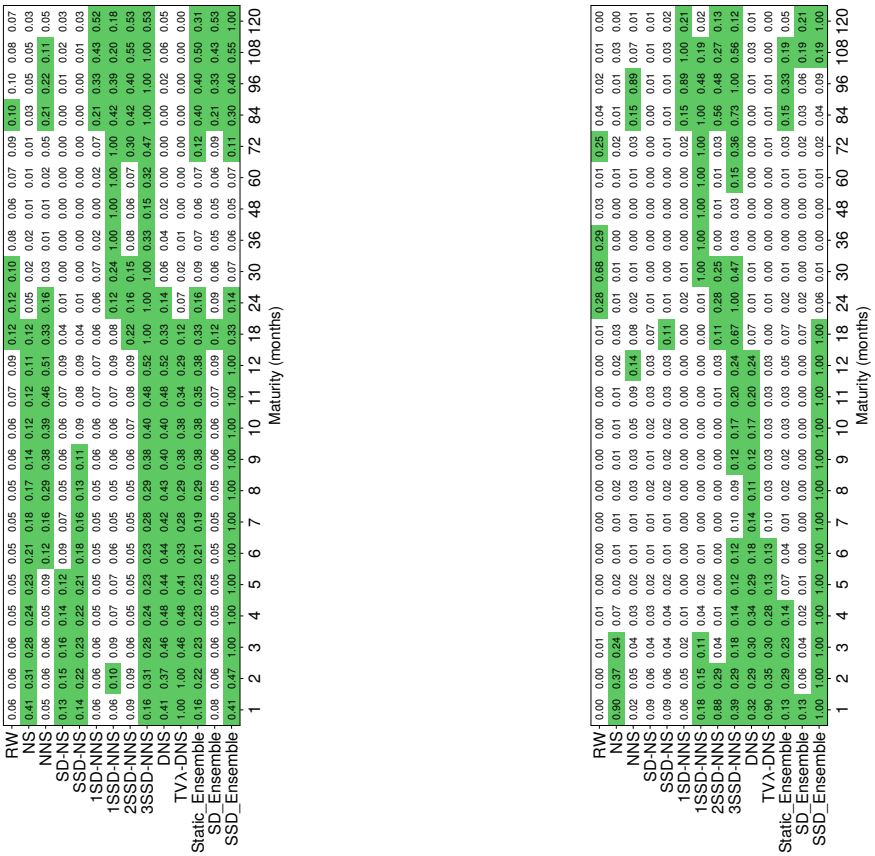

(a) aSPA (b) uSPA

FIGURE A1: MCS and p-values per maturity at significance level $\alpha_{MCS} = 0.1$ for $B = 999$ bootstrap samples

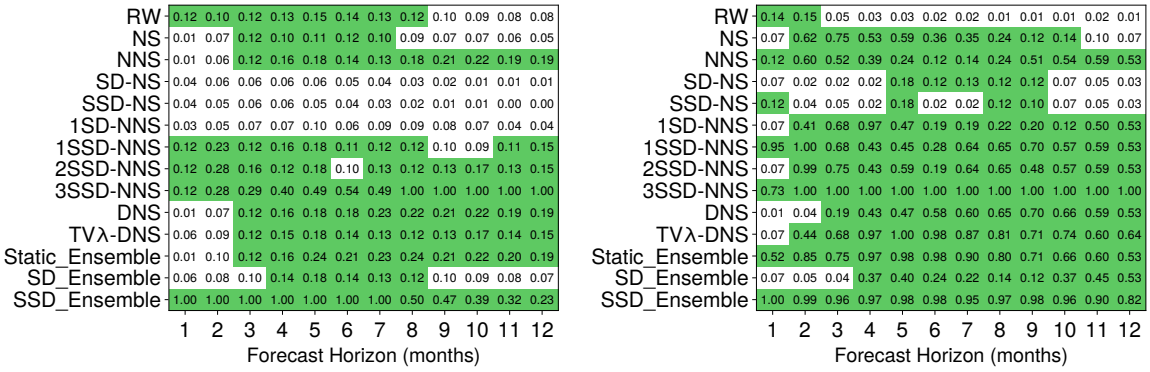

(a) aSPA (b) uSPA

FIGURE A2: MCS and p-values per forecast horizon at significance level $\alpha_{MCS} = 0.1$ for $B = 999$ bootstrap samples